frontiers | Frontiers in Earth Science

TYPE Original Research
PUBLISHED 24 September 2025
DOI 10.3389/feart.2025.1673352

OPEN ACCESS

EDITED BY
Yi Zheng,
Sun Yat-sen University, China

REVIEWED BY
Zhenwen Lin,
Guangdong Institute of Geological Survey, China
Shanling Fu,
Chinese Academy of Sciences, China

*CORRESPONDENCE
Hongjie Shen,
shenhongjie0627@qq.com

RECEIVED 25 July 2025
ACCEPTED 01 September 2025
PUBLISHED 24 September 2025

CITATION
Wang W, Shen H, Huang S, Shi J and Zhang Y (2025) Physicochemical constraints and fluid evolution pathways in skarn mineralization: insights from sphalerite geochemistry at the Dafang Pb–Zn–Au–Ag deposit, South China. *Front. Earth Sci.* 13:1673352. doi: 10.3389/feart.2025.1673352

Physicochemical constraints and fluid evolution pathways in skarn mineralization: insights from sphalerite geochemistry at the Dafang Pb–Zn–Au–Ag deposit, South China

Wusheng Wang[1], Hongjie Shen[2,3]*, Shihong Huang[1], Jian Shi[4] and Yu Zhang[2,3]

[1]Guiyang County Dafang Mining Co., Ltd., Chenzhou, China, [2]Key Laboratory of Metallogenic Prediction of Nonferrous Metals and Geological Environment Monitor (Central South University), Ministry of Education, Changsha, China, [3]School of Geosciences and Info-Physics, Central South University, Changsha, China, [4]Geospatial survey and monitoring institute of Hunan province, Changsha, China

Important Mid-Late Jurassic Pb–Zn polymetallic skarn deposits are widely distributed in South China, yet physiochemical conditions and migration of the ore-forming fluids in skarn deposits are poorly constrained. The Dafang Pb–Zn–Au–Ag deposit (38 kt Pb @ 1.4%, 33 kt Zn @ 1.3%, 6.1 t Au @ 1.80 g/t, and 370 t Ag @ 106.8 g/t) represents a typical skarn deposit in the South Hunan district, located at the intersection between the Nanling Region and the Qin-Hang Metallogenic Belt in South China. Its mineralization can be divided into four stages: (I) prograde skarn, (II) retrograde alteration, (III) quartz-sulfides, and (IV) carbonate-sulfides stages. Within the Dafang deposit, the primary Pb–Zn mineralization is prominently occurred in the principal calcite-sulfides stage (Stage IV). Within this stage, sphalerite exhibits distinct spatial distribution characteristics across three orebody types, allowing for its systematic classification into Sp-I (Orebody I), Sp-II (Orebody II), and Sp-III (Orebody III). This study investigates the textural characteristics and trace element geochemistry of these three sphalerite types to unravel the physicochemical conditions of mineralization and fluid pathways. Backscattered electron (BSE) imaging reveals that Sp-I, Sp-II, and Sp-III all display homogeneous internal textures and appear grayish-black. Detailed textural observations indicate that Sp-I is primarily associated with galena but is subsequently replaced by arsenopyrite, pyrite, and calcite. Sp-II is typically replaced by arsenopyrite and pyrite and hosts minor inclusions of chalcopyrite and stannite. Both Sp-III and coexisting galena are overprinted by pyrite, arsenopyrite, and calcite. Trace element analyses demonstrate two primary incorporation mechanisms within Dafang sphalerite: divalent cations (e.g., Fe^{2+}, Cd^{2+}, and Mn^{2+}) substitute directly for Zn^{2+} through isovalent substitution, while trivalent and tetravalent cations (e.g., Sb^{3+}, Ga^{3+}, In^{3+}, and Ge^{4+}) incorporate via charge-coupled substitution involving Cu^{+} and/or Ag^{+} to maintain electrostatic equilibrium. Crucially, the trace element geochemistry of Dafang sphalerite reveals a

progressive decrease in temperature and sulfur fugacity from Sp-III (~285 °C; lg fS_2 = −8.1 to −10.4, avg. −9.0) to Sp-II (~280 °C; lg fS_2 = −9.8 to −8.7, avg. −9.1) and subsequently to Sp-I (~279 °C; lg fS_2 = −9.5 to −9.3, avg. −9.4). This systematic variation in physicochemical conditions, particularly the spatially decreasing temperature gradient from NW to SE as indicated by the SPRFT geothermometer, suggests that ore-forming fluids migrated from the Lashuxia pluton towards the Maoerling pluton. This finding identifies the Lashuxia pluton as the primary metallogenic source, offering critical insights for the favorable target area for future exploration within the Dafang Pb–Zn–Au–Ag deposit.

KEYWORDS

sphalerite, trace element geochemistry, Dafang Pb–Zn–Au–Ag deposit, Lashuxia pluton, the South Hunan district

1 Introduction

Skarn deposits constitute a globally significant source of W–Sn, Pb–Zn–Ag, and Cu–Fe–Au mineralization (Einaudi et al., 1981; Meinert, 1992). The distinctive skarn mineral assemblages found within these deposits are intrinsically linked to the intricate interplay between magmatic activity and hydrothermal ore formation (Meinert et al., 2005). Among the sulfide minerals, sphalerite is a ubiquitous and economically vital component, particularly within skarn-type Pb–Zn systems, which typically form through the metasomatic interaction of magmatic-hydrothermal fluids with carbonate host rocks (Benedetto et al., 2005; Reich et al., 2005; Cook et al., 2009; Ma et al., 2022; Zhang et al., 2022; Frenzel et al., 2024; Shen et al., 2025). Importantly, the trace element geochemistry of sphalerite serves as a powerful proxy, widely employed to decipher the physicochemical evolution and reconstruct the complex ore-forming processes within skarn environments (Frenzel et al., 2016; Frenzel et al., 2021; Torró et al., 2023; Erlandsson et al., 2024; Frenzel and Thiele, 2024). Consequently, a comprehensive understanding of sphalerite's mineralogy, trace element partitioning, and formation conditions within skarn systems is paramount for both economic geology and the development of effective exploration strategies (Hutchison and Scott, 1981; Bonnet et al., 2016; Cugerone et al., 2020; Cugerone et al., 2024a; Cugerone et al., 2024b; Erlandsson et al., 2024; Erlandsson et al., 2024).

The Nanling Region and Qin-Hang Belt in South China are renowned metallogenic provinces characterized by a diverse array of skarn-type and vein-type polymetallic deposits (Figure 1; Shu et al., 2011). Notably, these belts host abundant Mid-Late Jurassic Pb–Zn skarn mineralization (Mao et al., 2013; Yuan et al., 2018a; Xiong et al., 2020). The South Hunan district (Figure 2), strategically situated at the intersection of the Nanling Region and Qin-Hang Belt (Li et al., 2017; Zhao et al., 2021; Zhao et al., 2022), represents a significant ore cluster, featuring numerous well-developed Mid-Late Jurassic Pb–Zn skarn deposits (Ding et al., 2022a; Ding et al., 2022b; Zhu et al., 2022; Tan et al., 2023; Tan et al., 2024). Prominent examples include the Baoshan Cu–Pb–Zn (calcite U–Pb: 158 ± 2 Ma; Zhang, 2023), Tongshanling Pb–Zn (cassiterite U–Pb: 162.6 ± 2.0 Ma; Wu et al., 2021), and Kangjiawan Pb–Zn (fuchsite ^{40}Ar–^{39}Ar: 158.1 ± 0.4 Ma; Shen et al., 2025) deposits. Numerous studies have been conducted on the geological, geochemical, and metallogenic characteristics of Pb–Zn skarn systems in the South Hunan district, providing valuable insights into their formation and evolution (e.g., Yuan et al., 2007; Yao et al., 2014; Li et al., 2023; Wang et al., 2023). However, despite the widespread occurrence and economic significance of these systems, the physicochemical conditions and migration of the ore-forming fluids remain insufficiently elucidated.

The Dafang Pb–Zn–Au–Ag deposit, boasting a proven ore reserve of 38 kt Pb @ 1.4%, 33 kt Zn @ 1.3%, 6.1 t Au @ 1.80 g/t, and 370 t Ag @ 106.8 g/t; Lu et al., 2017; Wang et al., 2021), is strategically situated within the South Hunan district, South China. The pervasive presence of multiple sphalerite generations within this deposit renders it an excellent natural laboratory for deciphering its mineralization history via sphalerite trace-element geochemistry. This study employs laser ablation inductively coupled plasma-mass spectrometry (LA-ICP-MS) for comprehensive trace-element profiling of sphalerite samples collected from diverse orebodies at Dafang, complemented by scanning electron microscope (SEM) backscattered electron (BSE) imaging to resolve textural complexities. Our primary objectives are to constrain the ore-forming physicochemical conditions (e.g., temperature and redox state) and their evolutionary trajectory, and furthermore, to elucidate the migration pathways of the ore-forming fluids. These critical insights will contribute significantly to a deeper understanding of ore genesis and provide targeted guidance for mineral exploration within analogous skarn environments.

2 Geological setting

2.1 Regional geology

The South China Block (SCB) comprises the Yangtze and Cathaysia blocks to the northwest and southeast, respectively, suturing along the Jiangshan-Shaoxing fault in the Neoproterozoic (Figure 1a; Zhao and Cawood, 2012). Internally, the SCB is amalgamated from the Yangtze Block (northwest) and the Cathaysia Block (southeast), a Neoproterozoic accretionary event demarcated by the Jiangshan–Shaoxing Fault (Figure 1a; Zhou et al., 2002; Hu et al., 2012). The SCB experienced widespread Mesozoic magmatism, resulting in the prolific development of granitic rocks. This magmatic activity occurred in distinct episodes: the Triassic (ca.

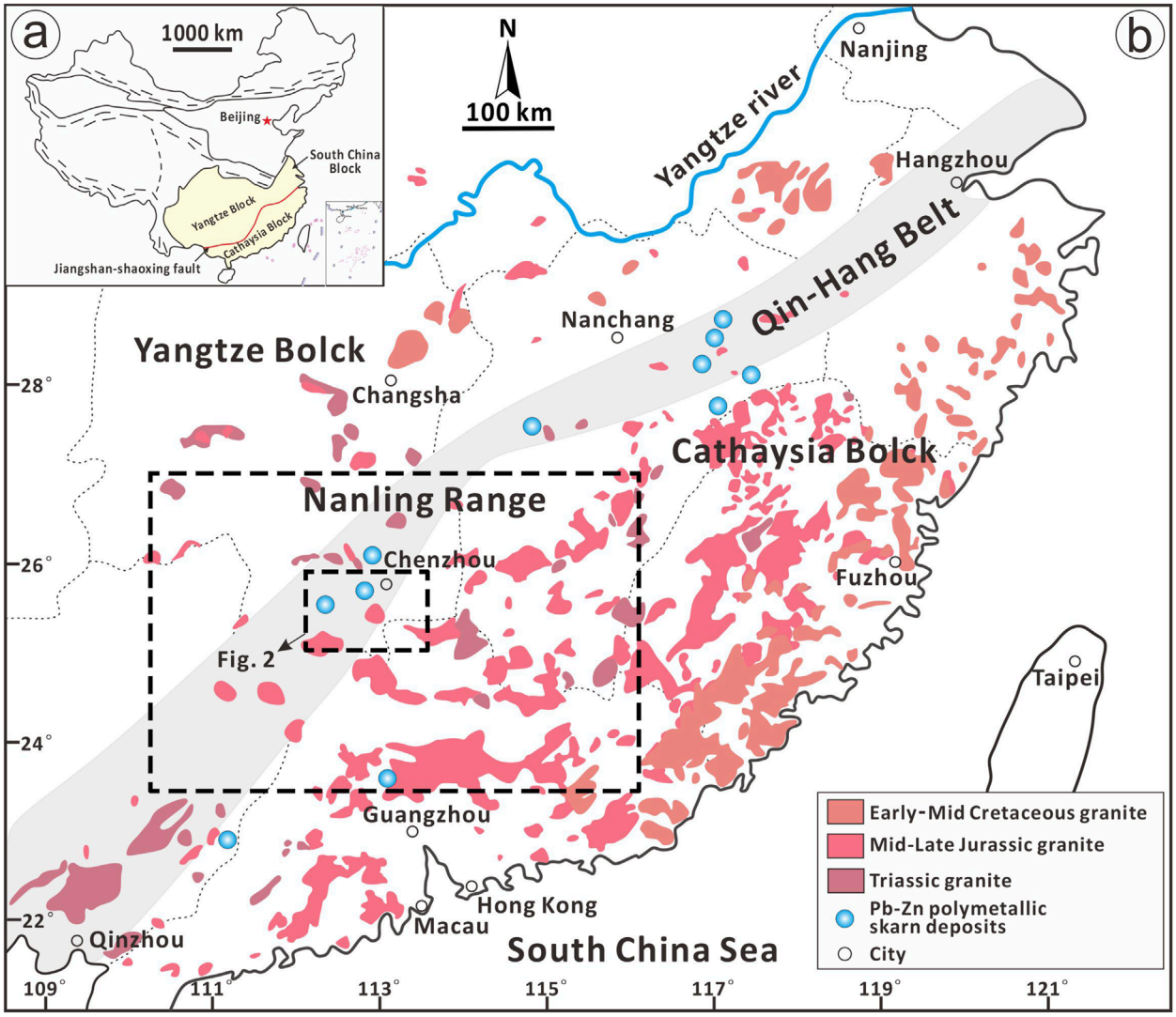

FIGURE 1
(a) Geologic map showing the location of South China in the Chinese mainland; **(b)** Locations of the Nanling Range and Qin-Hang Belt in South China (modified from Zhou et al., 2006; Mao et al., 2013).

251–205 Ma), Mid-Late Jurassic (ca. 180–142 Ma), and Cretaceous (ca. 140–66 Ma) (Zhou et al., 2006). These magmatic pulses are temporally and spatially correlated with three major metallogenic epochs (Mao et al., 2008; Mao et al., 2011; Mao et al., 2013). The initial mineralization event is constrained to the Late Triassic (230–210 Ma), followed by a subsequent phase during the Mid–Late Jurassic (170–150 Ma), and culminating with a final episode in the Early–Mid Cretaceous (120–80 Ma). Notably, the Mid-Late Jurassic tectonic-magmatic event was particularly significant. It gave rise to numerous porphyry-skarn Cu deposits along the Qin-Hang Belt, with formation ages typically ranging from 170 to 160 Ma. Concurrently, this event was responsible for the extensive formation of granite-related skarn W–Sn polymetallic deposits within the Nanling Region, primarily dated between 160 and 150 Ma (Mao et al., 2008; Mao et al., 2011; Mao et al., 2013).

The outcropping lithostratigraphic units in the South Hunan district are predominantly characterized by a sedimentary succession comprising Devonian–Triassic limestone and shale, Triassic–Neogene sandstone and siltstone, and Sinian–Cambrian slate and sandstone (Figure 2; Li et al., 2019). The geological evolution of South Hunan is marked by multi-stage tectonic episodes and associated magmatism. The regional basement complex, primarily consisting of severely metamorphosed pre-Silurian sedimentary rocks, was formed during and subsequent to the Caledonian orogeny (Late Silurian–Devonian). This orogenic event imposed dominant EW trending folds and EW/NE trending fault systems on the basement. These basement rocks, which serve as pivotal ore-hosting strata in the region, are unconformably overlain by a thick sequence of Devonian–Permian carbonate platforms. Subsequent to the Caledonian effects, the Indosinian orogeny (Triassic) generated a series of NS trending folds. Later, the Yanshanian orogeny (Jurassic–Cretaceous), driven by the rollback of the Paleo-Pacific subduction zone, superimposed the regional tectonics with the development of NNE-trending

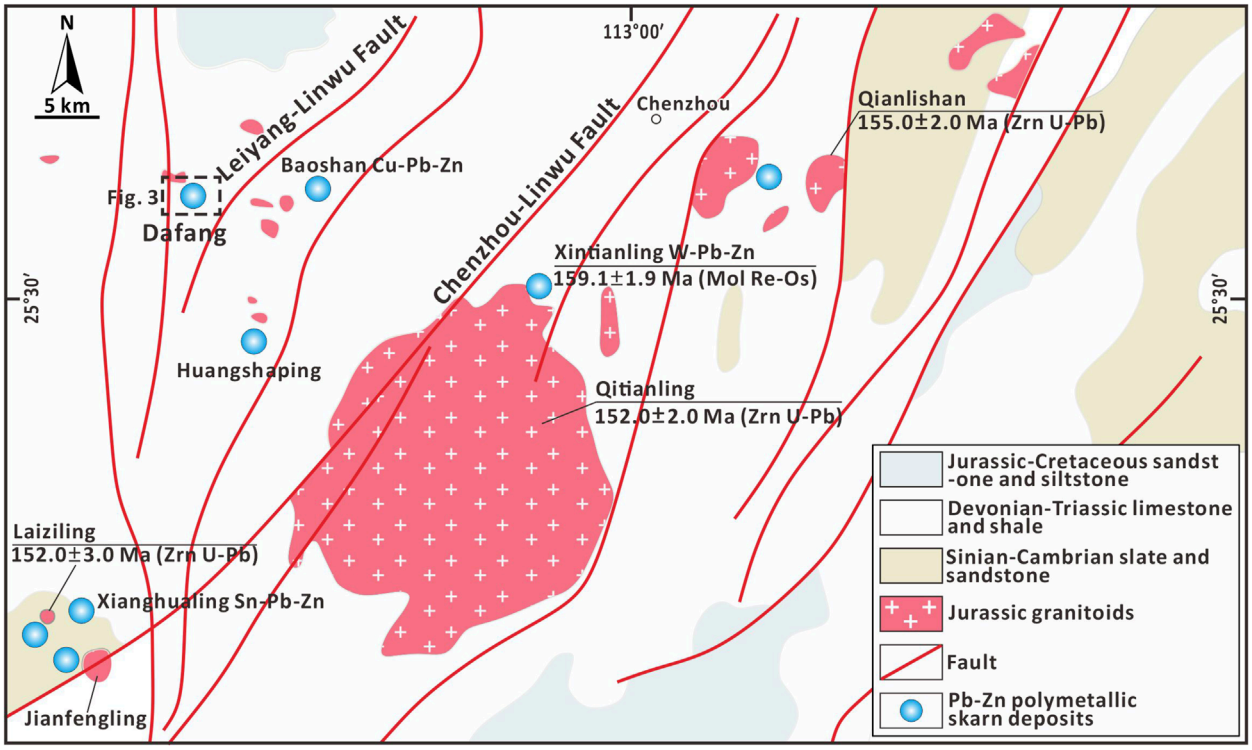

FIGURE 2
Geologic map of South Hunan district (after Li et al., 2019).

basin rifts and associated fault networks (Mao et al., 2007; Shu et al., 2004; Hu et al., 2017).

The South Hunan district experienced intense Yanshanian tectonism, which was contemporaneous with extensive Jurassic granitic magmatism. These granitoids, comprising granite and quartz porphyry, exhibit diverse intrusive morphologies including batholiths, laccoliths, stocks, and dikes (Figure 2; Li et al., 2019). The W–Sn polymetallic mineralization exhibits a genetic affiliation with highly fractionated S-type granites (159–155 Ma), which are petrologically defined by their reduced oxygen fugacity (fO_2), low H_2O content, seagull-shaped rare earth element (REE) patterns, and magmatic evolution dominated by fractional crystallization processes (Zhao et al., 2024). Representative examples include the Qianlishan pluton (157.0 ± 2.0 Ma; Chen et al., 2016) and Qitianling batholith (158.0 ± 1.1 Ma; Xia et al., 2024). In contrast, the Cu–polymetallic mineralization is genetically associated with I-type granodioritic intrusions (162–160 Ma), characterized by hydrous, oxidized magmatic signatures, listric-shaped REE patterns, and magmatic evolution primarily governed by partial melting processes (Zhao et al., 2022). The Baoshan stock (161.0 ± 1.3 Ma; Liu et al., 2020) and Tongshanling porphyry complex (161.4 ± 0.9 Ma; Wu et al., 2021) exemplify this mineralization style.

2.2 Deposit geology

The Dafang deposit is situated to the west of the Pingbao mining district, approximately 7 km from the well-known Baoshan Pb–Zn deposit. This polymetallic deposit primarily comprises two distinct ore zones: Maoerling and Lashuxia (Figure 3a; Wang et al., 2021; Wang et al., 2022; Chen et al., 2024). The stratigraphic successions exposed within the Dafang district are predominantly composed of Carboniferous and Permian sedimentary rocks. Specifically, the dominant host rocks for the Dafang Pb–Zn mineralization are the Lower Carboniferous dolomitic limestone and the Middle-Upper Carboniferous dolomite, which crop out in the western and central parts of the ore district, respectively (Figure 3b). The Lower Carboniferous unit is characterized by a thick sequence (approximately 500 m) of grey to dark, fine-grained dolomitic limestone. The upper sections of this stratum exhibit pervasive brittle deformation, leading to multi-stage fracturing. These fractures were subsequently infilled by iron-manganese minerals, resulting in distinctive breccia textures. Overlying this, the Middle-Upper Carboniferous formation consists of grey and greyish-white, medium-to fine-grained dolomite, occurring in thick, massive beds with a variable thickness ranging from 160 to 350 m (Figure 3a). To the eastern extent of the area, the stratigraphy transitions to exposed Lower Permian limestone and chert (silicalite), further overlain by Upper Permian sandstone (Jiang et al., 2024).

The mining district exhibits pervasive structural deformation, characterized by the extensive development of folds and faults (Figure 3a; Li and Li, 1983). The entire mineralized area is strategically positioned along the axial trace and limbs of the regional-scale Maopu-Zhangjiaping complex syncline (Wang et al., 2022). The axial trend of this complex syncline is oriented north-northeast, and it is internally differentiated by a series of subsidiary synclines and anticlines with near north-south orientations.

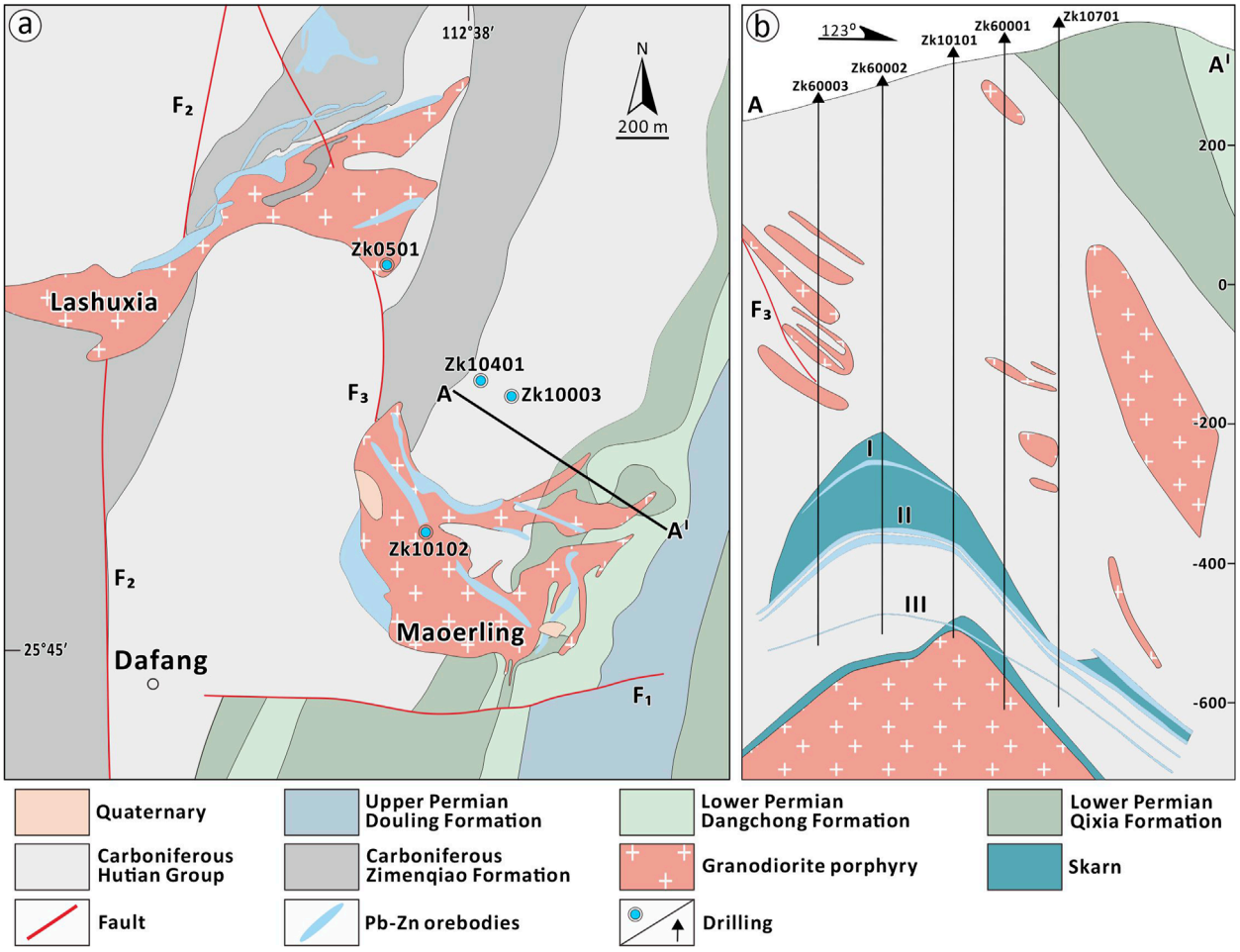

FIGURE 3
(a) Geologic map of the Dafang Pb–Zn–Au–Ag deposit (modified after Wang et al., 2021; Wang et al., 2022) and **(b)** geological cross-section of the Dafang deposit (modified after Chen et al., 2024).

Prominent secondary folds, from west to east, include the Maoerling and Lashuxia anticlines (Figure 3a). Previous structural mapping and field observations have identified four principal fault sets: EW, NS, NNW, and NWW-trending faults (Figure 3a). Specifically, the EW and WNW-trending faults (F_1, F_4) are interpreted as strike-slip or oblique-slip structures that have displaced Permian strata, resulting in juxtaposition between Lower Permian chert and Middle-Upper Carboniferous dolomite. An NS-trending fault (F_2) represents a reverse or thrust fault that has compressively uplifted Lower Carboniferous strata, emplacing them tectonically onto the Middle-Upper Carboniferous strata (Figure 3a). A significant NNW-trending fault system transects both the Maoershan and Lashuxia plutons, serving as a primary structural conduit for magmatic ascent and emplacement (Figure 3b). Subsequent to their intrusion, these igneous rocks interacted extensively with the adjacent Carboniferous sedimentary sequences, leading to the widespread development of significant skarn alteration. Furthermore, subsurface investigations, particularly through drill core analysis, reveal the presence of a network of blind faults that have caused partial fragmentation and dislocation of the orebodies (Zhang and Wang, 2023).

Within the mining district, two minor plutons are exposed at the surface, namely, the Lashuxia and Maoerling intrusions (Figure 3; Zhang et al., 2018). These intrusions manifest primarily as stocks and dikes, exhibiting a characteristic mushroom-like morphology that is broader at the top and tapers downwards, locally overlying the host dolomite. The predominant lithologies observed are granodiorite porphyry, with minor occurrences of granite porphyry and quartz porphyry. The Lashuxia pluton intruded along a northeast-trending fracture system. At the surface, it forms an elongated, sinuous, S-shaped dike with dips ranging from 50° to 65° to the southeast. The upper portion of this pluton displays prominent apophyses and sills, creating localized laccolithic or mushroom-like geometries before coalescing into a larger, more massive body at depth. Conversely, the Maoerling pluton was emplaced along a northwest-trending fracture. Its plunging orientation is towards the northwest, with a dip to the northeast. The upper contact surface of this intrusion is relatively steep, plunging at angles of 60°–80°, while its lower section exhibits a gentler dip of 30°–50°. The exposed surface of the pluton is elliptical in plain view, and it attenuates at depth into an irregular, vein-like structure characterized by numerous branching bifurcations. Deep drilling data further indicate the

presence of a larger, concealed pluton at depth. These individual plutonic components are interconnected in the subsurface via apophyses and composite intrusive structures (Wang et al., 2022). Geochronological dating indicates that the granodiorite porphyry in the Dafang mining area was emplaced at 155.0 ± 2.0 Ma and 154.5 ± 1.0 Ma (Zhang et al., 2018), aligning with the primary tectono-magmatic activity phase in South Hunan.

The Dafang Pb–Zn–Au–Ag deposit is geologically delineated into two primary mining sectors: Maoerling and Lashuxia, each exhibiting distinctive horizontal zonation of mineralization (Figure 3a). The broader mining district hosts four major orebodies alongside 84 minor ones, which occur predominantly as vein-type, lenticular, or stratiform morphologies. Superficial orebodies within the oxidation zone are typically observed within 30 m of the surface. In the Maoerling sector, orebodies are distributed across two principal elevation ranges: from −40 m to 300 m and from −350 m to 80 m (Figure 3b), indicating a significant vertical extent of mineralization. Conversely, in the Lashuxia sector, orebodies are largely concentrated within an elevation range of 150 m–300 m, with significantly attenuated mineralization encountered below 150 m (Li and Li, 1983). A majority of the ore bodies are preferentially localized within the contact aureole between the granodiorite porphyry intrusions and the country rocks, typically assuming vein- or lenticular geometries (Figure 3b). Notably, orebodies I, II, and III are classified as vein-type and lenticular Pb–Zn mineralization, primarily situated along the hinge zones of regional folds, suggesting a strong structural control on ore deposition (Figure 3b).

Detailed field geologic and petrographic observations at the Dafang deposit reveal a complex and diverse assemblage of metallic and non-metallic minerals, which provide critical insights into the mineralization processes and paragenetic sequence. The primary metallic minerals include pyrrhotite, pyrite, arsenopyrite, chalcopyrite, galena, sphalerite, native gold, tetrahedrite, and stannite (Lu et al., 2017; Wu et al., 2021). These minerals exhibit distinct textural relationships and modes of occurrence: pyrrhotite and pyrite form massive aggregates and disseminated grains, often associated with arsenopyrite and chalcopyrite; galena and sphalerite occur as vein infillings or replacements, frequently intergrown with tetrahedrite and stannite; native gold is commonly observed as fine grains within pyrite and chalcopyrite, indicating a close genetic relationship. The non-metallic mineral assemblage is dominated by calc-silicates, including garnet, diopside, epidote, tremolite, and actinolite, accompanied by chlorite, sericite, muscovite, biotite, quartz, and calcite (Wang et al., 2021; Wang et al., 2022; Zhang and Wang, 2023; Chen et al., 2024). Garnet and diopside are predominant in the prograde skarn stage, forming euhedral to subhedral crystals with distinct zonation, while epidote, actinolite, and chlorite characterize the retrograde alteration stage, typically replacing earlier-formed calc-silicates. Quartz and calcite are pervasive throughout the deposit, often associated with sulfide mineralization. Hydrothermal alteration of the wall rocks is marked by the development of garnet, sericite, quartz, and calcite (Wang et al., 2021; Wang et al., 2022; Chen et al., 2024). Garnet occurs as coarse-grained crystals in the skarn zones, while sericite and quartz form fine-grained aggregates along fractures and grain boundaries. Calcite is ubiquitous, often filling vugs and fractures in association with sulfides (Chen et al., 2024).

Based on a comprehensive analysis of mineral assemblages and textural relationships (Wang et al., 2021; Wang et al., 2022; Zhang and Wang, 2023; Chen et al., 2024), four distinct stages of mineralization have been identified (Figure 4): (I) Prograde skarn formation, dominated by garnet and diopside, reflects high-temperature metasomatic processes; (II) Retrograde alteration, characterized by the development of actinolite, epidote, and chlorite, signifies a transition to lower-temperature conditions; (III) Quartz-sulfides stage, marked by the precipitation of quartz, pyrite, and chalcopyrite, represents the principal phase of sulfide mineralization; and (IV) Calcite-sulfides stage, involving the deposition of calcite alongside a diverse suite of sulfides, including pyrite, chalcopyrite, arsenopyrite, sphalerite, and galena, corresponding to the terminal stages of mineralization.

3 Sampling and analytical methods

3.1 Samples

For this investigation, a total of 64 representative ore samples were systematically collected from 15 core drill holes, specifically designated as ZK0501, ZK6001, ZK6002, ZK10101, ZK10102, ZK10002, ZK10003, ZK10201, ZK10301, ZK10401, ZK10801, ZK11102, ZK11103, ZK60001, and ZK60701. Subsequent to collection, 40 polished thin sections were meticulously prepared for detailed petrographic examination under both transmitted and reflected light microscopy. From the broader collection, 18 sphalerite-bearing ore samples, originating specifically from Orebodies I, II, and III (corresponding to the Stage V: calcite-sulfides mineralization event), were carefully selected for comprehensive textural and geochemical analyses. For the *in-situ* trace-element microanalysis of sphalerite, a subset of these samples, including DF6-1, DF6-3, DF6-5, DF8-1, DF8-3, DF12-1, DF12-5, DF13-2, DF15-6, and DF20-1, were specifically chosen. A detailed lithological and mineralogical description for each sample is comprehensively presented in Table 1.

3.2 SEM-BSE imaging

Prior to the LA-ICP-MS analyses, each sample underwent meticulous preparation, involving the creation of highly polished thin sections. The internal textures and microstructures of sphalerite were subsequently characterized using a JCM-7000 scanning electron microscope (SEM), housed at the School of Geosciences and Info-Physics, Central South University (Changsha, China). During SEM operation, an accelerating voltage of 15 kV and a beam current of 10 nA were precisely maintained to ensure optimal imaging and analytical resolution.

3.3 LA-ICP-MS sphalerite trace element analysis

In-situ trace element analysis of sphalerite was meticulously conducted using an NWR 193 nm ArF excimer laser ablation system coupled to an iCAP RQ Inductively Coupled Plasma-Mass

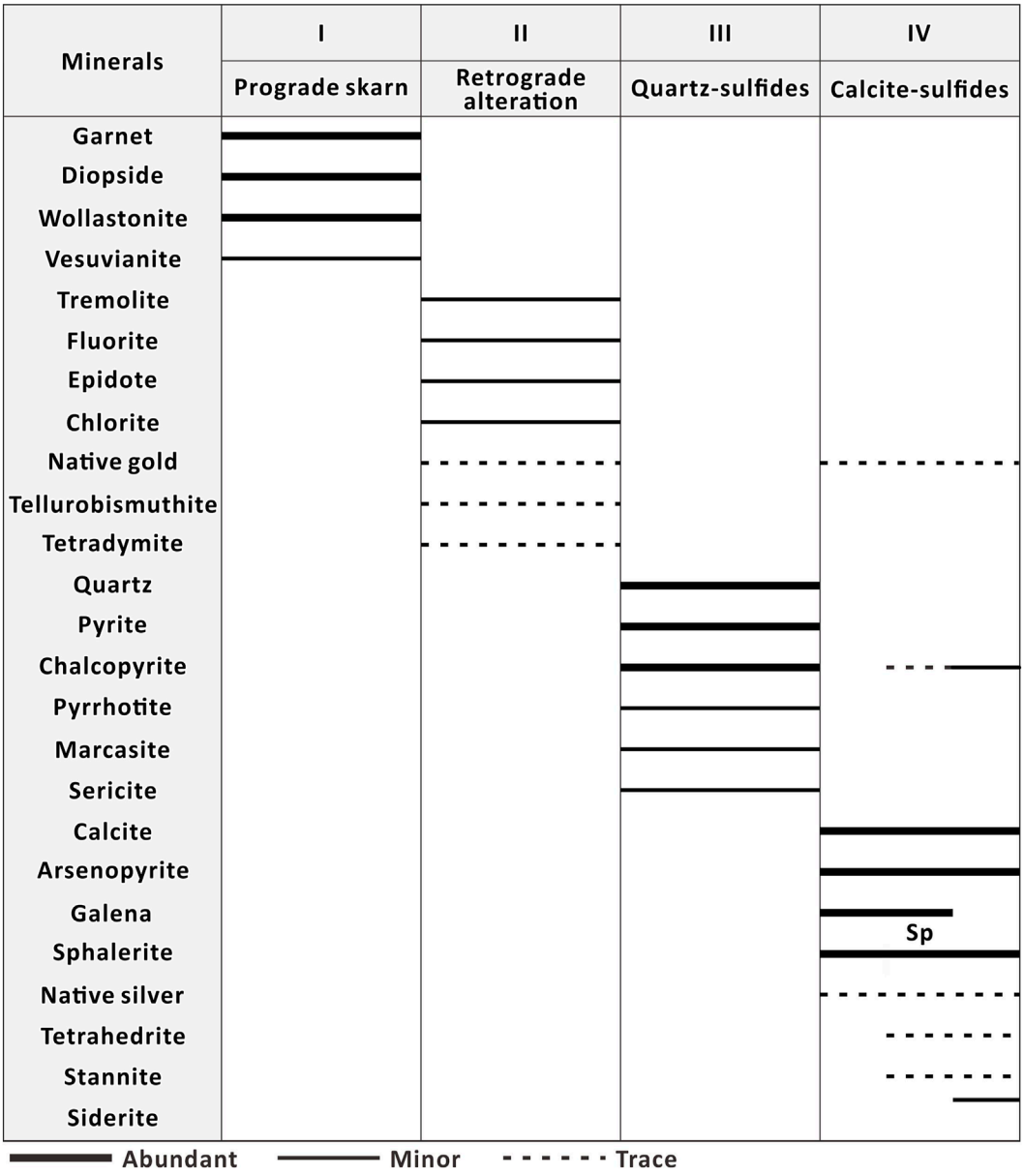

FIGURE 4
Paragenetic sequence alteration and mineralization assemblages at Dafang (modified after Wang et al., 2021; Wang et al., 2022; Chen et al., 2024).

Spectrometer (LA-ICP-MS) at the Guangzhou Tuoyan Analytical Technology Co. Ltd. Prior to each ablation, all target spots were carefully scrutinized under BSE mode to precisely identify and avoid contamination from mineral inclusions. Helium (He) was employed as the carrier gas to efficiently transport the ablated aerosol into the ICP and to minimize aerosol deposition within the transport tubing. The laser parameters were precisely set as follows: a laser fluence of 3.5 J/cm^2, a repetition rate of 6 Hz, and a laser spot size of 30 μm. Each analytical spot involved a total acquisition time of 80 s, comprising a 15-s pre-ablation period for background signal acquisition, a 40-s ablation period for sample signal measurement, and a 25-s post-ablation period for residual signal acquisition. For pyrite analysis, the following 19 isotopes were precisely measured: ^{34}S, ^{55}Mn, ^{57}Fe, ^{59}Co, ^{60}Ni, ^{65}Cu, ^{66}Zn, ^{75}As, ^{77}Se, ^{97}Mo, ^{107}Ag, ^{118}Sn, ^{121}Sb, ^{126}Te, ^{197}Au, ^{202}Hg, ^{205}TL, ^{208}Pb, and ^{209}Bi. Similarly, for sphalerite analysis, a distinct suite of 19 isotopes was quantified: ^{34}S, ^{55}Mn, ^{57}Fe, ^{59}Co, ^{60}Ni, ^{65}Cu, ^{66}Zn, ^{71}Ga, ^{74}Ge, ^{77}Se, ^{97}Mo, ^{107}Ag, ^{111}Cd, ^{115}In, ^{118}Sn, ^{121}Sb, ^{126}Te, ^{208}Pb, and ^{209}Bi. Data reduction and calibration were performed using Iolite software (Paton et al., 2011). Within this software, user-defined time intervals were precisely established for the baseline correction procedure, facilitating the calculation of session-wide baseline-corrected values for each measured isotope. The analytical sequence rigorously followed a protocol where blocks of two certified reference materials (NIST 610 and GSE-2G) and one sulfide matrix-matched standard (MASS-1) analysis were interspersed with measurements of 5 to 8 unknown samples, ensuring robust quality control and calibration.

TABLE 1 Descriptions of representative samples of sulfides at Dafang.

Sample no.	Orebody no.	Mineral assemblages	Stage	Description
DF6-1	II	Py-Gn-Sp	IV	Calcite-bearing massive pyrite-galena-sphalerite ore
DF6-3	II	Cal-Py-Gn-Sp	IV	Massive pyrite ore with large amounts of sphalerite
DF6-5	II	Py-Gn-Sp	IV	Euhedral-subhedral sphalerite intergrown with galena and pyrite
DF8-1	II	Cal-Py-Gn-Sp	IV	Abundant sphalerite replaced pyrite
DF8-3	I	Py-Gn-Sp	IV	Euhedral-subhedral pyrite replaced with galena and sphalerite
DF9-2	I	Apy-Py-Sp	IV	Massive arsenopyrite-pyrite-sphalerite ore
DF12-1	III	Py-Gn-Sp	IV	Abundant pyrite replaced by sphalerite
DF12-3	II	Py-Gn-Sp	IV	Sphalerite intergrown with calcite and galena
DF12-4	II	Gn-Sp	IV	Massive galena-sphalerite ore
DF12-5	I	Apy-Py-Gn-Sp	IV	Massive arsenopyrite-pyrite-galena-sphalerite ore
DF13-2	II	Qz-Py-Sp	IV	Minor quartz intergrown with galena and sphalerite
DF15-5	II	Py-Po-Gn-Sp	IV	Stage IV pyrite intergrown with pyrrhotite but replaced by galena and sphalerite
DF15-6	II	Gn-Sp	IV	Massive calcite-sphalerite-galena ore
DF17-2	I	Apy-Gn-Sp	IV	Euhedral-subhedral arsenopyrite replaced by sphalerite
DF17-4	I	Apy-Gn-Sp	IV	Massive arsenopyrite-galena-sphalerite ore
DF17-7	III	Py-Gn-Sp	IV	Massive pyrite ore with large amounts of sphalerite and galena
DF20-1	III	Cal-Apy-Py-Gn-Sp	IV	Euhedral-subhedral sphalerite intergrown with galena but replaced arsenopyrite
DF22-3	III	Qz-Py-Gn-Sp	IV	Euhedral-subhedral galena and sphalerite intergrown with quartz

Abbreviations: Apy = arsenopyrite; Py = pyrite; Gn = galena; Sp = sphalerite; Po = pyrrhotite; Cal = calcite; Qz = quartz.

4 Results

4.1 Internal texture of sphalerite

Sphalerite-I (Sp-I), interpreted to have formed within Orebody I, appears dark-gray in backscattered electron (BSE) images and typically exhibits a homogeneous internal texture, devoid of discernible zoning or replacement features (Figures 5a,b); this sphalerite is commonly observed intergrown with galena (Figure 5b) but frequently undergoes subsequent pervasive replacement by abundant calcite (Figure 5a) and minor arsenopyrite and pyrite (Figure 5b). In contrast, Sphalerite-II (Sp-II), associated with Orebody II, also presents as grayish-black in BSE images and is texturally homogeneous (Figures 5c,d), commonly showing evidence of pervasive replacement by arsenopyrite and pyrite (Figure 5c) and often hosting minor inclusions of chalcopyrite and stannite (Figure 5d). Finally, Sphalerite-III (Sp-III), originating from Orebody III, appears dark-grey and texturally homogeneous under BSE (Figures 5e,f), commonly associated with galena but extensively replaced by a suite of later-forming minerals, including pyrite (Figures 5e,f), arsenopyrite (Figure 5f), and calcite (Figures 5e,f).

4.2 Trace element geochemistry

A comprehensive suite of 50 LA-ICP-MS spot analyses was conducted on the three distinct sphalerite generations: Sp-I (n = 15), Sp-II (n = 25), and Sp-III (n = 10). The detailed trace-element compositions are tabulated in Supplementary Appendix I and graphically presented in Figure 6. Notably, Sp-III exhibits the highest median concentrations for several key elements, including Fe (115170 ppm), Ge (1.37 ppm), Ag (42.9 ppm), Cd (14865 ppm), and Sb (2.88 ppm). In contrast, Sp-I is characterized by elevated median contents of Mn (31520 ppm), Ga (13.2 ppm), Ag (31.7 ppm), and Sn (34.5 ppm). Conversely, when compared to Sp-II, Sp-I consistently shows lower median concentrations for a range of elements: Fe (105554 ppm), Co (2.18 ppm), Ni (below detection limit), Cu (1277 ppm), As (below detection limit), Se (23.1 ppm), In (9.93 ppm), Cd (13474 ppm), Sb (1.69 ppm), Te (0.121 ppm), Pb (3.52 ppm), and Bi (0.011 ppm).

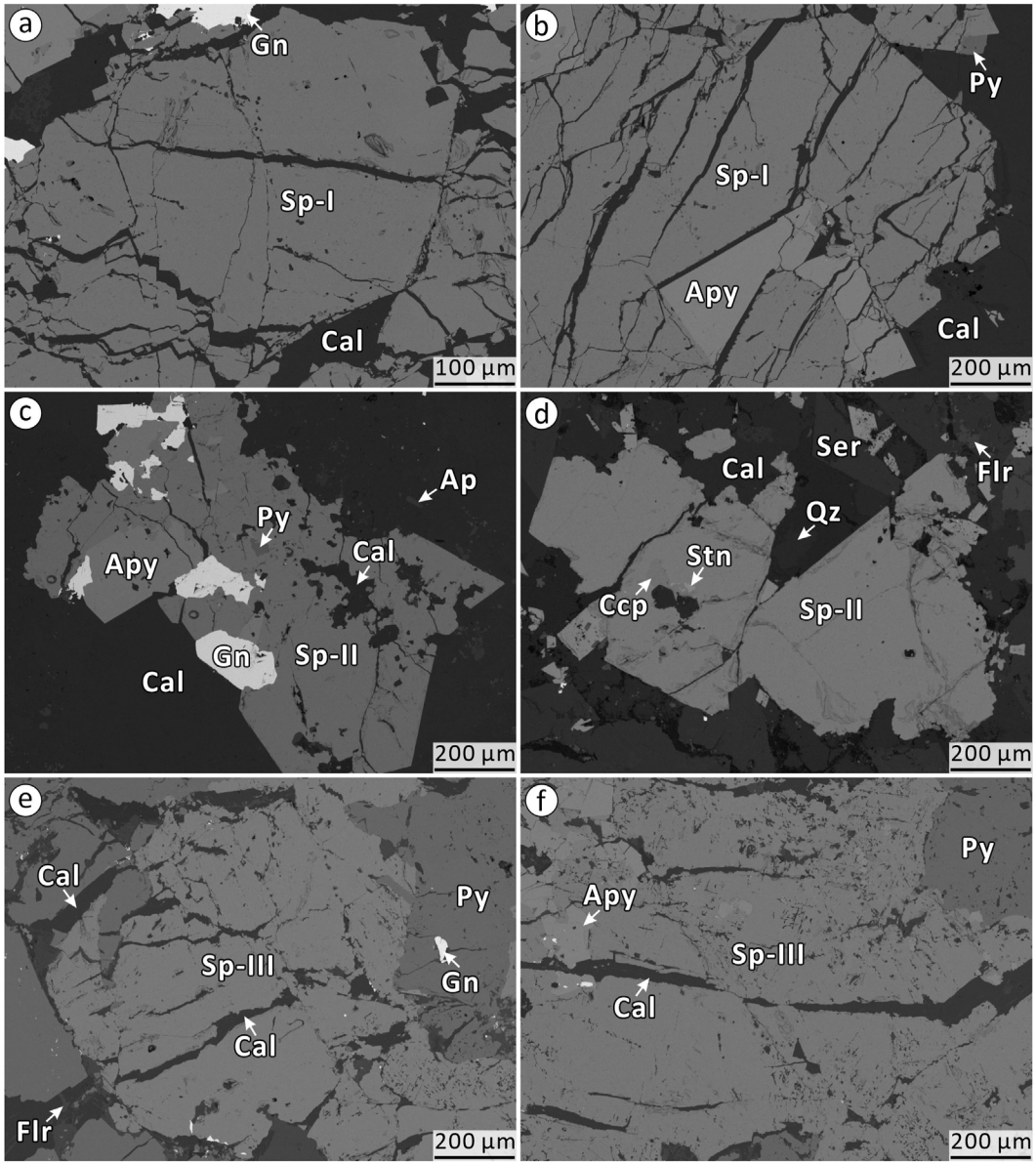

FIGURE 5
Representative BSE images of the Dafang sphalerite grains: **(a,b)** dark-gray Sp-I with homogeneous (no zoning or replacement) texture, and intergrown with galena but replaced calcite, arsenopyrite, and pyrite; **(c,d)** grayish-black Sp-II with homogeneous texture, and replaced by arsenopyrite and pyrite and hosting chalcopyrite-stannite inclusions; **(e,f)** Sp-III (dark-grey and texturally homogeneous) commonly associated with galena but replaced by pyrite, arsenopyrite, and calcite. Abbreviations: Sp = sphalerite.

5 Discussion

5.1 Trace element occurrence in sphalerite

Sphalerite is frequently observed to host micro-/nano-inclusions (e.g., Johan et al., 1983; Cook et al., 2009; 2016; Duan et al., 2023; Fougerouse et al., 2023), a phenomenon that can mask the true geochemical compositions of the host mineral (Fontboté et al., 2017; Voute et al., 2019; Keith et al., 2022). Consequently, a critical evaluation of the influence of these nano-inclusions on the overall sphalerite geochemistry is imperative. LA-ICP-MS time-resolved signal spectra serve as a valuable tool for discerning the occurrence and distribution of trace elements within sphalerite (Belousov et al., 2016; Shen et al., 2025). For Sp-I, Sp-II, and Sp-III, the time-resolved signals for Fe, Mn, Cd, In, and Sb exhibit smooth and flat profiles (Figure 7), strongly suggesting the absence of corresponding micro-inclusions in the Dafang sphalerite. However, the presence of outliers in box-and-whisker plots may signify the existence of evenly-distributed nano-inclusions that are beyond the spatial resolution of LA-ICP-MS (Keith et al., 2022; Shen et al., 2022; Zhang et al., 2022). This interpretation is supported by the elevated concentrations (outliers) of As, Ag, and Sn in Sp-I, and Fe, Ge, As, Ag, Sn, Te, and Pb in Sp-II (Figure 6), indicating the potential presence of nano-inclusions enriched in these specific

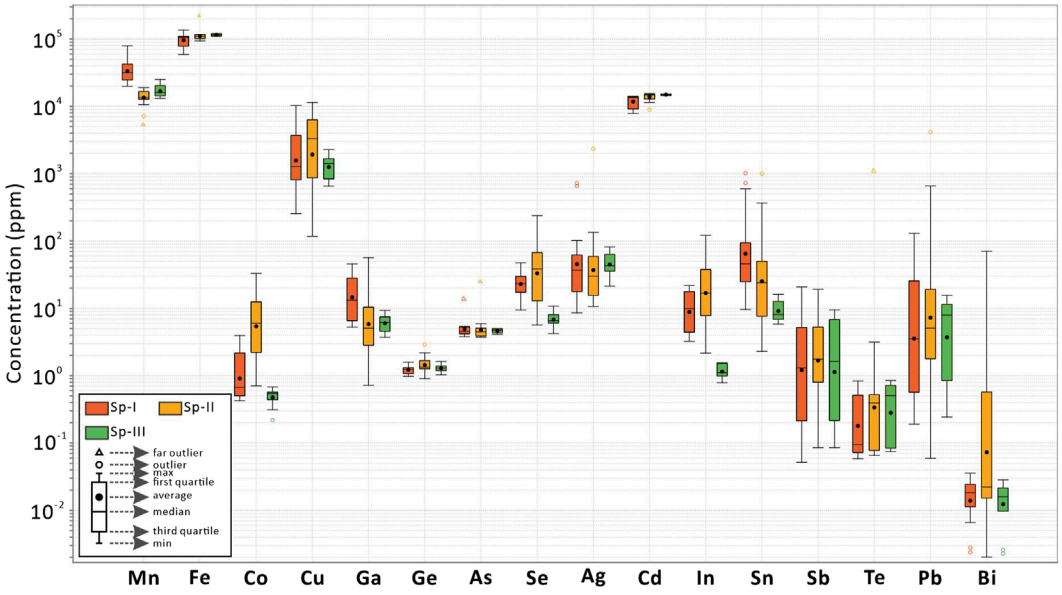

FIGURE 6
Box and whisker plot for trace element contents of the three sphalerite types from Dafang.

elements within these sphalerite types. Further corroboration comes from local signal peaks for Pb, Sn, Sb (Figure 7b), Cu, and Ag (Figures 7d,e) observed in the time-resolved data. Concurrently, the broad concentration ranges for Sn and Pb in both Sp-I and Sp-II (Figure 6) provide additional evidence for the occurrence of such micro-inclusions (Shen et al., 2022; Zhang et al., 2022), an observation consistent with the textural evidence of their coexistence with stannite (Figure 5d).

Building upon well-established theoretical frameworks, bivalent cations such as Fe^{2+}, Mn^{2+}, Cd^{2+}, Co^{2+}, Ni^{2+}, and Hg^{2+} are widely understood to directly substitute for Zn^{2+} within the sphalerite crystal lattice (e.g., Barton and Toulmin, 1966; Pattrick et al., 1998; Cook et al., 2009; Frenzel et al., 2020; 2022). Conversely, the incorporation of trivalent and tetravalent cations, including Sb^{3+}, Ga^{3+}, In^{3+}, Sn^{3+}, Ge^{4+}, and Pb^{4+}, is predominantly facilitated by coupled substitution involving Cu^{+} and/or Ag^{+} replacing Zn (Cook et al., 2012; Belissont et al., 2014; Belissont et al., 2016; George et al., 2016; Frenzel et al., 2016). Following the rigorous filtering of geochemical outliers from the sphalerite samples, our data reveal a positive correlation between (Fe + Cd + Mn) and Zn (Figure 8a), strongly indicating that Fe, Cd, and Mn are readily incorporated into the sphalerite structure through isovalent substitution for Zn. In contrast, the suite of Ga–Ge–In–Sn–Sb elements appear to be integrated into the sphalerite lattice primarily via coupled substitution mechanisms. This is demonstrably evidenced by the positive correlations observed between Ga and (Cu + Ag) (Figure 8b), Ge and Ag (Figure 8c), Sn and Cu (Figure 8d), Sb and Cu (Figure 8e), and comprehensively between (Ga + Ge + In + Sn + Sb) and (Cu + Ag) (Figure 8f). Furthermore, the consistent plotting of almost all data points above the (Ga + Ge + In + Sn + Sb)/(Cu + Ag) = 1:1 line (Figure 8f) provides additional compelling support for these coupled substitution pathways.

5.2 Physicochemical conditions of the Dafang mineralization

5.2.1 Temperature

The geochemical composition and internal textures of sphalerite serve as invaluable proxies for deciphering the physicochemical conditions and ore-forming processes within hydrothermal deposits (Frenzel et al., 2016; 2021; Torró et al., 2023; Erlandsson et al., 2024; Frenzel and Thiele, 2024). Generally, high-temperature sphalerite is characterized by enrichment in Fe, Mn, Cu, Co, In, and Sn, exhibiting high In/Ga (>1) and Zn/Cd (>500) ratios, alongside low Zn/Fe (<100) ratios. Conversely, low-temperature sphalerite typically shows enrichment in Ga, Ge, and Cd, with corresponding low In/Ge (<1) and Zn/Cd (100–500) ratios, and high Zn/Fe (>100) ratios (Liu et al., 1984; Ye et al., 2011; Dai, 2016; Wen et al., 2016; Wei et al., 2018; Wei et al., 2019; Bauer et al., 2019). Applying these established indicators, our observations reveal that Sp-III is notably richer in Fe and Mn and exhibits a lower Zn/Fe ratio (4.42) compared to Sp-II (4.86), suggesting a higher crystallization temperature for Sp-III. Furthermore, Sp-II, being enriched in Fe, Cu, and In, displays higher In/Ga (avg. 7.00), In/Ge (avg. 22.87), and a lower Zn/Fe ratio (avg. 4.86) than Sp-I (0.76, 7.10, and 5.57, respectively), which points to Sp-II crystallizing at a higher temperature than Sp-I. Crucially, the significantly higher concentrations of Co, Ni, Se, and Bi in Sp-II (avg. 6.01, 12.7, 38.6, and 1.06 ppm, respectively) compared to Sp-I (avg. 2.18, below detection limit, 23.1, and 0.011 ppm, respectively), further corroborate a temperature decline from Sp-II to Sp-I. This is consistent with the understanding that magmatic fluids, often contributing to higher temperature mineralization, generally contain elevated levels of Se, Bi (Huston et al., 1995; Rowins et al., 1997; Fitzpatrick, 2008; Li et al., 2018; Zhang et al., 2022), Co, and Ni (Loftus-Hills and

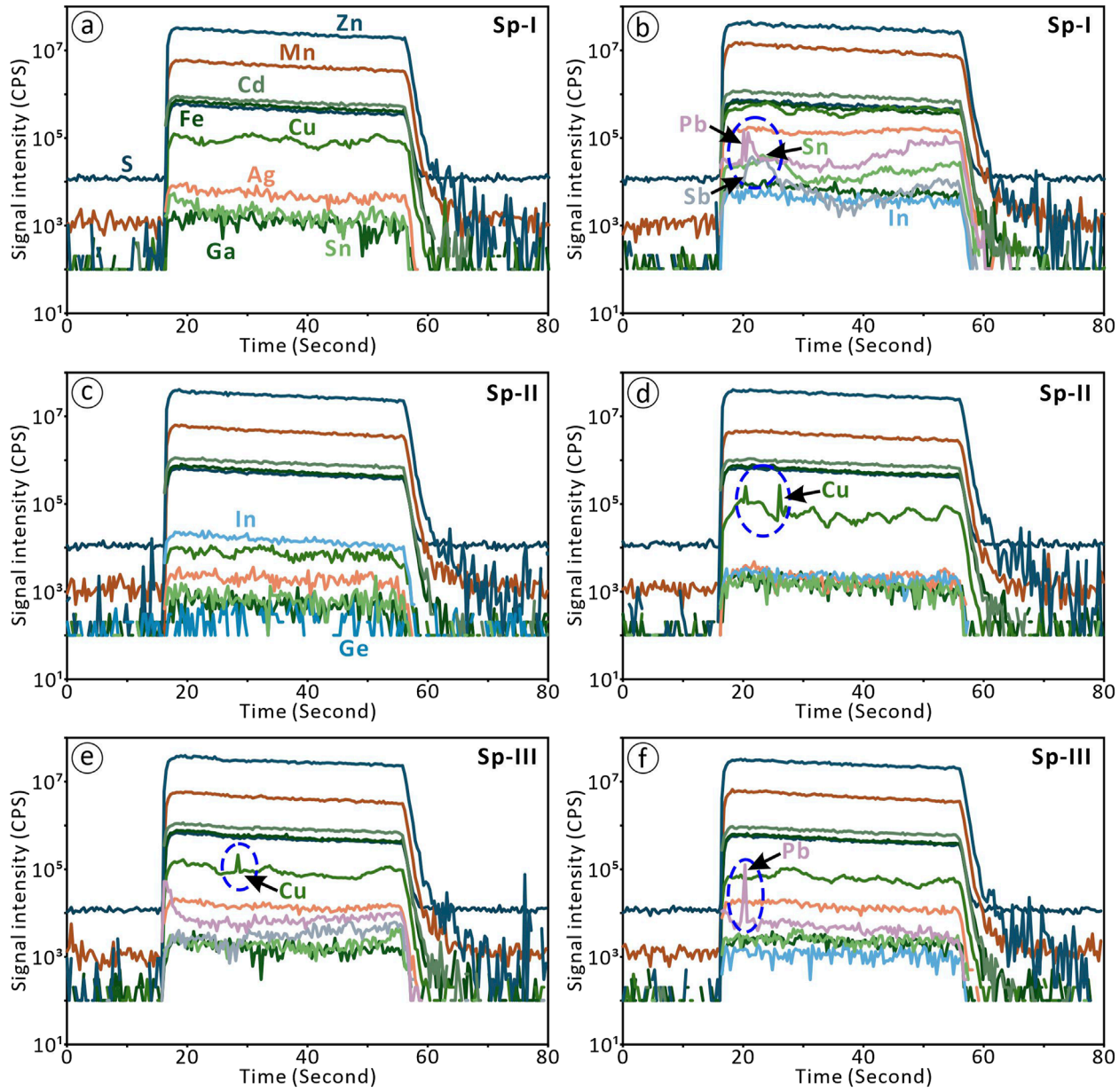

FIGURE 7
Representative LA-ICP-MS time-resolved depth profiles for the Dafang sphalerite. **(a)** Sp-I displays smooth ablation signals for Zn, S, Fe, Cd, Mn, Cu, Ag, Ga, and Sn; **(b)** Sp-I shows local signal peaks of Pb, Sn, and Sb; **(c)** Sp-II exhibits smooth ablation signals for Zn, S, Fe, Cd, Mn, Cu, Ag, Ga, Sn, In, and Ge; **(d)** Sp-II contains local signal peaks of Cu; **(e)** Sp-III presents local signal peaks of Cu; **(f)** Sp-III shows local signal peaks of Pb. Abbreviations: Zn = zinc; S = sulfur; Fe = iron; Cd = cadmium; Mn = manganese; Ga = gallium; Cu = copper; Ag = silver; Sn = tin; Pb = lead; Sb = antimony; In = indium; Ge = germanium.

Solomon, 1967; Bralia et al., 1979; Chen et al., 1987) compared to meteoric waters.

Sphalerite crystallization temperatures were also quantitatively assessed using the GGIMFis (Frenzel et al., 2016) and SPRFT (Zhao et al., 2024) geothermometers. The GGIMFis thermometer yielded medium-high temperatures for Sp-I (avg. 347 °C), Sp-II (avg. 349 °C), and Sp-III (avg. 341 °C), which are inconsistent with published quartz fluid inclusion microthermometric data (Stage IV: 150°C–294 °C; Wang et al., 2022). However, the crystallization temperature calculated by the SPRFT geothermometer (Zhao et al., 2024) indicated medium-low crystallization temperatures for Sp-I (~279 °C), Sp-II (~280 °C), and Sp-III (~285 °C), which are consistent with the published quartz fluid inclusion microthermometric data (Wang et al., 2022). Therefore, it is inferred that the crystallization temperature of sphalerite gradually decreased from Sp-III to Sp-II and then to Sp-I, a trend supported by both the trace element geochemistry of sphalerite and the consistent results from the SPRFT geothermometer.

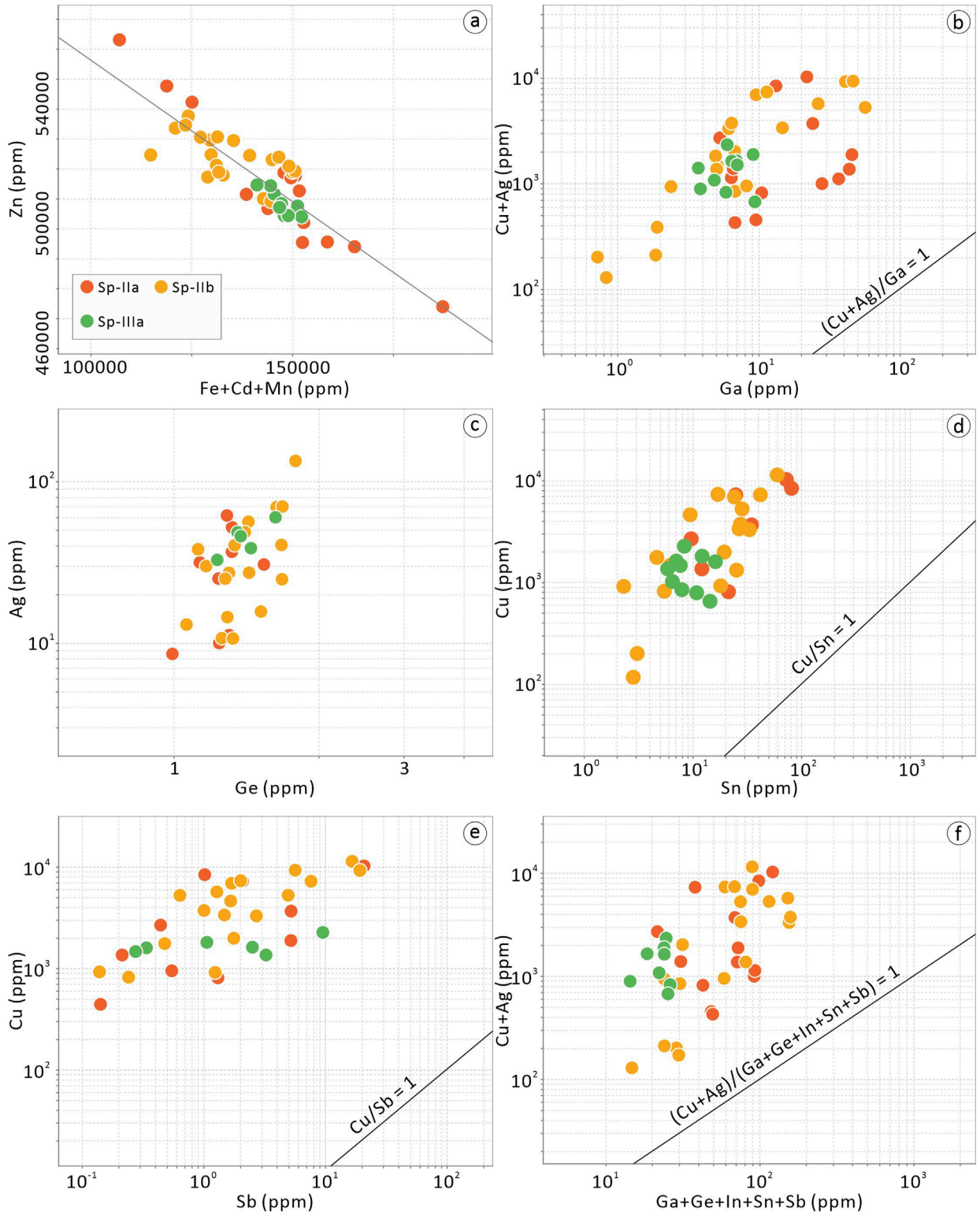

FIGURE 8
Binary plots of **(a)** Zn vs. (Fe + Cd + Mn); **(b)** (Cu + Ag) vs. Ga; **(c)** Ge vs. Ag; **(d)** Cu vs. Sn; **(e)** Cu vs. Sb; **(f)** (Cu + Ag) vs. (Ga + Ge + In + Sn + Sb) for the Dafang sphalerite.

5.2.2 Sulfur fugacity (fS_2)

Iron incorporation into the sphalerite crystal lattice is controlled by both temperature and sulfur fugacity (fS_2) (Scott and Barnes, 1971; Keith et al., 2014; Schaarschmidt et al., 2021; Frenzel et al., 2016; Frenzel et al., 2022). While fS_2 can theoretically be estimated using the sphalerite formation temperature (e.g., via

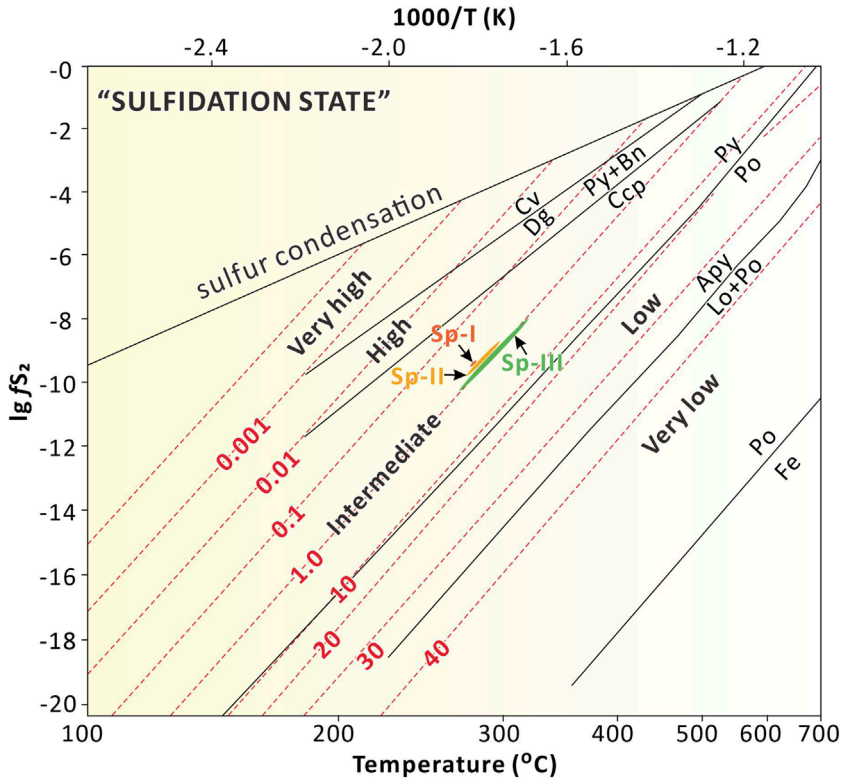

FIGURE 9
Temperature vs. lg fS_2 diagram adapted from Einaudi et al. (2003). Calculated temperatures from the SPRFT geothermometry (Zhao et al., 2024) and fluid inclusion microthermometric data (Wang et al., 2022) are compared with the sphalerite FeS content. The blue and green areas denote the fS_2 field for Sp2 and Sp3, respectively. Abbreviations: Cv = covellite; Dg = digenite; Py = pyrite; Bn = bornite; Ccp = chalcopyrite; Po = Pyrrhotite; Apy = arsenopyrite; Lo = löllingite; Fe = native iron.

the GGIMFis geothermometer; Frenzel et al., 2016) and FeS mol%, the unreliability of temperature data calculated by the GGIMFis geothermometer necessitates an alternative approach. Therefore, published fluid inclusion microthermometric data (Stage IV: 150 °C–294 °C; Wang et al., 2022) were utilized to constrain fS_2. Based on these constraints, the calculated fS_2 values for Sp-I (lg fS_2 = −9.5 to −9.3, avg. −9.4), Sp-II (lg fS_2 = −9.8 to −8.7, avg. −9.1), and Sp-III (lg fS_2 = −8.1 to −10.4, avg. −9.0) all fall within the intermediate-sulfidation field (Figure 9). More specifically, these results reveal a progressive decrease in fS_2 from Sp-III to Sp-II, and subsequently to Sp-I.

5.2.3 Oxygen fugacity (fO_2)

Manganese concentrations within sphalerite are highly sensitive indicators of redox conditions (Bernardini et al., 2004; Kelley et al., 2004), with elevated Mn typically signifying a more reduced environment (Kelley et al., 2004; Zhuang et al., 2019; Liu et al., 2022). The lower median Mn content observed in Sp-II (13767 ppm) compared to Sp-III (16053 ppm) suggests an evolution of the ore-forming fluids towards more oxidizing conditions from orebody III to II. Conversely, the notable increase in Mn content from Sp-II to Sp-I (median: 31520 ppm) points to a subsequent decrease in oxygen fugacity (fO_2). This late-stage reduction in fO_2 is likely attributable to the precipitation of galena (PbS) and sphalerite (ZnS) through the reaction of Pb^{2+} and Zn^{2+} with H_2S. This mineralization process consumes H_2S and concurrently releases H^+ (e.g., Zn^{2+} + $H_2S \rightarrow ZnS + 2H^+$), thereby reducing the overall concentration of dissolved sulfide species (H_2S/HS^-) and promoting a more reduced state within the system.

5.3 Migration of the ore-forming fluids

The migration of ore-forming fluids is a pivotal process in the genesis of skarn Pb–Zn deposits, fundamentally controlling the spatial distribution, morphology, and economic tenor of mineralization. Understanding the pathways, drivers, and evolution of these fluid systems is crucial for both robust deposit modeling and effective exploration targeting. From the perspective of vertical spatial distribution, the ore-forming fluids exhibit a significant temperature gradient during their ascent (Figure 3B). Based on published quartz fluid inclusion microthermometric data (Stage IV: 150 °C–294 °C; Wang et al., 2022) and sphalerite thermometry using the SPRFT geothermometer (Zhao et al., 2024), crystallization temperatures systematically decrease from the deep orebody III (approx. 285 °C) to the middle orebody II (approx. 280 °C) and subsequently to the shallow orebody I (approx. 279 °C). This consistent temperature-decreasing sequence unequivocally indicates the upward migration path of ore-forming fluids from deeper to shallower crustal levels. Additionally, the progressive decrease in sulfur fugacity (fS_2) from Sp-III (avg. lg fS_2 = −9.0) to Sp-II (avg. lg fS_2 = −9.1) and then to Sp-I (avg. lg fS_2 = −9.4) (Figure 9), as well as the redox evolution reflected

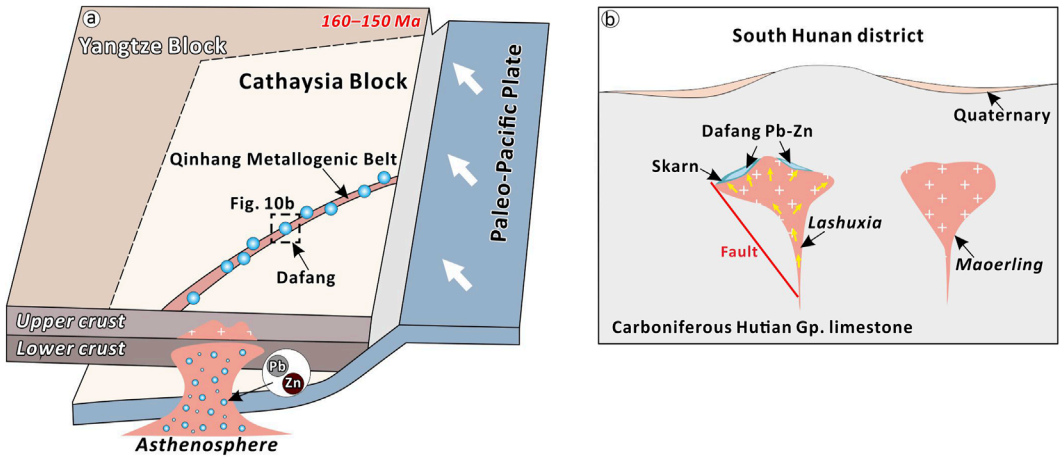

FIGURE 10
Schematic model illustrating the ore-forming processes at the Dafang Pb–Zn deposit (modified after Mao et al., 2013). **(a)** The upwelling of asthenospheric magma and extensive mantle–crust interaction, potentially induced by the slab window, likely contributed to the formation of Pb–Zn polymetallic deposits in this upwelling region around 160–150 Ma; **(b)** The magmatic hydrothermal fluids from the Lashuxia granodiorite porphyry migrated along faults and ultimately led to the formation of the Dafang Pb–Zn mineralization. See text for detailed discussion. Abbreviations: Zn = zinc; Pb = lead; Gp. = group.

by Mn concentrations in sphalerite (Figure 6), further corroborate this migration pathway.

Regarding planar distribution, sphalerite formation temperatures calculated by the SPRFT geothermometer from different drill cores also exhibit regular variations. Specifically, temperatures progressively decrease from drill hole ZK0501 (283 °C) to ZK10401 (281 °C), then to ZK10003 (280 °C), and finally to ZK10102 (275 °C), defining a discernible temperature gradient zone that trends from northwest to southeast (Figure 3a). Integrated with regional geological context, this spatial characteristic of the temperature field strongly suggests that the ore-forming fluids likely originated from the Lashuxia pluton in the northwest and migrated along structural conduits towards the Maoerling pluton in the southeast. The systematic variations in sphalerite trace element compositions (e.g., Fe, Mn, Co, Ni, Se, Bi; Figure 6) across the different orebodies further support this interpretation, reflecting changes in fluid chemistry during migration. Integrating the foregoing analytical results with existing geochronological constraints (calcite U–Pb: 157.7 ± 6.5 Ma; Wang et al., 2022), we interpret the Dafang Pb–Zn mineralization as a Middle–Late Jurassic event genetically associated with a slab-window regime induced by shallow oblique subduction of the paleo-Pacific Plate beneath the Eurasian continental margin (Figure 10a; Mao et al., 2008; Mao et al., 2013). This tectonic configuration facilitated asthenospheric magma upwelling, thereby supplying both the thermal energy and metal-rich fluids essential for ore genesis. Geochemical signatures of sphalerite further reveal a pronounced temporal, spatial, and genetic correlation between the Pb–Zn mineralization and the proximal Lashuxia granodiorite porphyry (Figure 10b), suggesting their coeval formation within a unified magmatic–hydrothermal ore-forming system.

This discovery holds significant implications for mineral exploration: Firstly, the spatial variation pattern of the temperature field, combined with fS_2 and fO_2 trends, provides reliable thermodynamic and geochemical evidence for determining the migration direction of ore-forming fluids. Secondly, by integrating the characteristics of temperature gradient variation with the spatial distribution of plutons, it is preliminarily concluded that the Lashuxia pluton is more likely the primary ore-forming parent rock of the Dafang Pb–Zn–Au–Ag deposit, rather than the traditionally considered Maoerling pluton (Wang et al., 2021; Wang et al., 2022). This understanding has important theoretical value for guiding deep and peripheral exploration in the mining area. It is recommended that subsequent exploration efforts focus on structurally favorable locations around the Lashuxia pluton.

6 Conclusion

The Pb–Zn mineralization at Dafang is primarily associated with the calcite-sulfides stage (Stage IV), with sphalerite classified into three types—Sp-I, Sp-II, and Sp-III—based on their spatial distribution across orebodies I, II, and III, respectively. Detailed BSE imaging and mineralogical analysis reveal that Sp-I, Sp-II, and Sp-III exhibit homogeneous textures but distinct paragenetic associations. Sphalerite geochemistry demonstrates that divalent cations (e.g., Fe^{2+}, Mn^{2+}) substitute directly for Zn^{2+} in the crystal lattice, while trivalent and tetravalent cations incorporate via charge-coupled substitution involving Cu^{+} and/or Ag^{+} to maintain electrostatic equilibrium. Geochemical and thermodynamic modeling shows a progressive decrease in temperature and sulfur fugacity from Sp-III (~285 °C) to Sp-II (~280 °C) and Sp-I (~279 °C), indicating fluid evolution. Temperature gradients suggest ore-forming fluids migrated from the Lashuxia pluton to the Maoerling pluton, identifying Lashuxia as the primary metallogenic source and challenging traditional views. These findings advance understanding of skarn Pb–Zn deposit genesis and provide a framework for

exploration targeting, emphasizing structurally favorable zones around the Lashuxia pluton for future exploration.

Data availability statement

The original contributions presented in the study are included in the article/Supplementary Material, further inquiries can be directed to the corresponding author.

Author contributions

WW: Conceptualization, Formal Analysis, Investigation, Project administration, Resources, Software, Writing – original draft, Writing – review and editing. HS: Conceptualization, Data curation, Resources, Software, Validation, Writing – original draft, Writing – review and editing. SH: Conceptualization, Data curation, Software, Validation, Writing – review and editing. JS: Formal Analysis, Funding acquisition, Supervision, Visualization, Writing – review and editing. YZ: Funding acquisition, Methodology, Visualization, Writing – review and editing.

Funding

The author(s) declare that financial support was received for the research and/or publication of this article. This research was funded by the scientific research project of Geological Bureau of Hunan Province (HNGSTP202456).

Acknowledgments

Special thanks are given to Guangzhou Tuoyan Analytical Technology Co. Ltd. for helping with the LA–ICP–MS trace element analysis.

Conflict of interest

Authors WW and SH were employed by Guiyang County Dafang Mining Co., Ltd.

The remaining authors declare that the research was conducted in the absence of any commercial or financial relationships that could be construed as a potential conflict of interest.

Generative AI statement

The author(s) declare that no Generative AI was used in the creation of this manuscript.

Any alternative text (alt text) provided alongside figures in this article has been generated by Frontiers with the support of artificial intelligence and reasonable efforts have been made to ensure accuracy, including review by the authors wherever possible. If you identify any issues, please contact us.

Publisher's note

Supplementary material

The Supplementary Material for this article can be found online at: https://www.frontiersin.org/articles/10.3389/feart.2025.1673352/full#supplementary-material

References

Barton, P. B., and Toulmin, P. (1966). Phase relations involving sphalerite in the Fe-Zn-S system. *Econ. Geol.* 61, 815–849. doi:10.2113/gsecongeo.61.5.815

Bauer, M. E., Burisch, M., Ostendorf, J., Krause, J., Seifert, T., Gutzmer, J., et al. (2019). Trace element geochemistry of sphalerite in contrasting hydrothermal fluid systems of the Freiberg district, Germany: insights from LA-ICP-MS analysis, near-infrared light microthermometry of sphalerite-hosted fluid inclusions, and sulfur isotope geochemistry. *Miner. Deposita* 52, 237–262. doi:10.1007/s00126-018-0850-0

Belissont, R., Boiron, M., Luais, B., and Cathelineau, M. (2014). LA-ICP-MS analyses of minor and trace elements and bulk Ge isotopes in zoned Ge-rich sphalerites from the Noailhac-Saint-Salvy deposit (France): insights into incorporation mechanisms and ore deposition processes. *Geochimica Cosmochimica Acta* 126, 518–540. doi:10.1016/j.gca.2013.10.052

Belissont, R., Muñoz, M., Boiron, M. C., Boiron, M. C., Luais, B., and Mathon, O. (2016). Distribution and oxidation state of Ge, Cu and Fe in sphalerite by μ-XRF and K-edge μ-XANES: insights into Ge incorporation, partitioning and isotopic fractionation. *Geochimica Cosmochimica Acta* 177, 298–314. doi:10.1016/j.gca.2016.01.001

Belousov, I., Large, R. R., Meffre, S., Danyushevsky, L. V., Steadman, J., and Beardsmore, T. (2016). Pyrite compositions from VHMS and orogenic Au deposits in the Yilgarn Craton, Western Australia: implications for gold and copper exploration. *Ore Geol. Rev.* 79, 474–499. doi:10.1016/j.oregeorev.2016.04.020

Benedetto, F. D., Bernardini, G. P., Costagliola, P., Plant, D., and Vaughan, D. J. (2005). Compositional zoning in sphalerite crystals. *Am. Mineralogist* 90, 1384–1392. doi:10.2138/am.2005.1754

Bernardini, G. P., Borgheresi, M., Cipriani, C., Di Benedetto, F., and Romanelli, M. (2004). Mn distribution in sphalerite: an EPR study. *Phys. Chem. Minerals* 31, 80–84. doi:10.1007/s00269-003-0374-7

Bonnet, J., Mosser-Ruck, R., Caumon, M. C., Rouer, O., Andre-Mayer, A. S., Cauzid, J., et al. (2016). Trace element distribution (Cu, Ga, Ge, Cd, and Fe) in sphalerite from the Tennessee MVT deposits, USA, by combined EMPA, LA-ICP-MS, Raman Spectroscopy, and Crystallography. *Can. Mineralogist* 54 (5), 1261–1284. doi:10.3749/canmin.1500104

Bralia, A., Sabatini, G., and Troja, F. (1979). A revaluation of the Co/Ni ratio in pyrite as geochemical tool in ore genesis problems. *Miner. Deposita* 14, 353–374. doi:10.1007/bf00206365

Chen, G. Y., Sun, D. S., and Yin, H. A. (1987). *Genetic mineralogy and mineral mineralogy*. Chongqing, China: Chongqing Publishing Group, 35–41. (in Chinese with English abstract).

Chen, Y. X., Li, H., Sun, W. D., Ireland, T., Tian, X. F., Hu, Y. B., et al. (2016). Generation of late mesozoic Qianlishan A2-type granite in nanling range, South China: implications for Shizhuyuan W–Sn mineralization and tectonic evolution. *Lithos* 266, 435–452. doi:10.1016/j.lithos.2016.10.010

Chen, X., Wang, Z. K., Yu, P. P., Wu, Y. H., Huang, Y., Tan, Z. J., et al. (2024). Physicochemical condition of the Dafang skarn Au-Ag-Zn-Pb polymetallic deposit in the Nanling Metallogenic Belt (South China), a perspective from sphalerite mineralogy and geochemistry. *Ore Geol. Rev.* 165, 105923. doi:10.1016/j.oregeorev.2024.105923

Cook, N. J., Ciobanu, C. L., Pring, A., Skinner, W., Shimizu, M., Danyushevsky, L., et al. (2009). Trace and minor elements in sphalerite: a LA-ICPMS study. *Geochimica Cosmochimica Acta* 73, 4761–4791. doi:10.1016/j.gca.2009.05.045

Cook, N. J., Ciobanu, C. L., Brugger, J., Etschmann, B., Howard, D. L., De Jonge, M. D., et al. (2012). Determination of the oxidation state of Cu in substituted Cu In-Fe-bearing sphalerite via μ-XANES spectroscopy. *Am. Mineralogist* 97, 476–479. doi:10.2138/am.2012.4042

Cook, N. J., Ciobanu, C. L., George, L., Zhu, Z. Y., Wade, B., and Ehrig, K. (2016). Trace element analysis of minerals in magmatic-hydrothermal ores by laser ablation inductively coupled plasma mass spectrometry: approaches and opportunities. *Minerals* 6, 111–134. doi:10.3390/min6040111

Cugerone, A., Cenki-Tok, B., Oliot, E., Muñoz, M., Barou, F., Motto-Ros, V., et al. (2020). Redistribution of germanium during dynamic recrystallization of sphalerite. *Geology* 48 (3), 236–241. doi:10.1130/g46791.1

Cugerone, A., Salvi, S., Kouzmanov, K., Laurent, O., and Cenki, B. (2024a). Tracing fluid signature and metal mobility in complex orogens: insights from Pb-Zn mineralization in the Pyrenean Axial Zone. *Miner. Deposita* 60, 955–977. doi:10.1007/s00126-024-01329-5

Cugerone, A., Oliot, E., Muñoz, M., Barou, F., Motto-Ros, V., and Cenki, B. (2024b). Plastic deformation and trace element mobility in sphalerite. *Am. Mineralogist* 109, 1888–1912. doi:10.2138/am-2023-9215

Dai, H. Z. (2016). *Geological and geochemical characteristics and metallogenetic mechanism of the Taiping Pb–Zn deposit, Yunnan province*. Beijing: China University of Geosciences.

Ding, T., Tan, T., Wang, J., Ma, D., Lu, J., Zhang, R., et al. (2022a). Trace-element composition of pyrite in the Baoshan Cu–Mo–Pb–Zn deposit, southern Hunan Province, China: insights into the ore genesis. *Ore Geol. Rev.* 147, 104989. doi:10.1016/j.oregeorev.2022.104989

Ding, T., Tan, T., Wang, J., Ma, D., Lu, J., Zhang, R., et al. (2022b). Multiple sources for the Baoshan polymetallic Cu–Mo–Pb–Zn deposit, southern Hunan Province, China: insights from *in situ* LA–MC–ICP–MS sulfur isotopic compositions. *Ore Geol. Rev.* 143, 104808. doi:10.1016/j.oregeorev.2022.104808

Duan, H. Y., Wang, C. M., Hu, R., Zhu, J. X., and Deng, J. (2023). Supernormal enrichment of cadmium in sphalerite via coupled dissolution-reprecipitation process. *Commun. Earth Environ.* 4 (1), 356–359. doi:10.1038/s43247-023-01025-8

Einaudi, M. T., Meinert, L. D., and Newberry, R. J. (1981). Skarn deposits. Economic geology. *75th Anniv.* Volume, 317–391. doi:10.5382/AV75.11

Einaudi, M. T., Hedenquist, J. W., and Inan, E. E. (2003). *Sulfidation state of fluids in active and extinct hydrothermal systems: transition from porphyry to epithermal environments*, 10. Littleton, CO: Society of Economic Geologists, 285–313.

Erlandsson, V. B., Foltyn, K., Muchez, P., Rantitsch, G., Ellmies, R., and Melcher, F. (2024). Chalcopyrite, sphalerite, and pyrite chemistry in stratiform sediment-hosted Cu(-Co) metallogenic districts: trace element characteristics and factors controlling polymetallic mineralization. *Miner. Deposita*, 1–26. doi:10.2138/am-2022-8636

Fitzpatrick, A. J. (2008). *The measurement of the Se/S ratios in sulfide minerals and their application to ore deposit studies*. Canada: Queen's University, 203.

Fontboté, L., Kouzmanov, K., Chiaradia, M., and Pokrovski, G. S. (2017). Sulfide minerals in hydrothermal deposits. *Elements* 13, 97–103. doi:10.2113/gselements.13.2.97

Fougerouse, D., Cugerone, A., Reddy, S. M., Luo, K., and Motto-Ros, V. (2023). Nanoscale distribution of Ge in Cu-rich sphalerite. *Geochimica Cosmochimica Acta* 346, 223–230. doi:10.1016/j.gca.2023.02.011

Frenzel, M., and Thiele, S. T. (2024). Deceptively critical sphalerite. *Nat. Geosci.* 17, 1199. doi:10.1038/s41561-024-01587-y

Frenzel, M., Hirsch, T., and Gutzmer, J. (2016). Gallium, germanium, indium, and other trace and minor elements in sphalerite as a function of deposit type-a meta-analysis. *Ore Geol. Rev.* 76, 52–78. doi:10.1016/j.oregeorev.2015.12.017

Frenzel, M., Cook, N. J., Ciobanu, C. L., Slattery, A. D., Wade, B. P., Gilbert, S., et al. (2020). Halogens in hydrothermal sphalerite record origin of ore-forming fluids. *Geology* 48, 766–770. doi:10.1130/g47087.1

Frenzel, M., Voudouris, P., Cook, N. J., Ciobanu, C. L., Gilbert, S. E., and Wade, B. (2021). Evolution of a hydrothermal ore-forming system recorded by sulfide mineral chemistry: a case study from the Plaka Pb–Zn–Ag Deposit, Lavrion, Greece. *Miner. Deposita* 57, 417–438.

Frenzel, M., Voudouris, P., Cook, N. J., Ciobanu, C. L., Gilbert, S. E., and Wade, B. (2022). Evolution of a hydrothermal ore-forming system recorded by sulfide mineral chemistry: a case study from the Plaka Pb–Zn–Ag Deposit, Lavrion, Greece. *Miner. Deposita* 57, 417–438. doi:10.1007/s00126-021-01067-y

Frenzel, M., Röhner, M., Cook, N. J., Gilbert, S., Ciobanu, C. L., and Güven, J. F. (2024). Mineralogy, mineral chemistry, and genesis of Cu-Ni-As-rich ores at Lisheen, Ireland. *Miner. Deposita* 60, 113–143. doi:10.1007/s00126-024-01299-8

George, L., Cook, N. J., and Ciobanu, C. L. (2016). Partitioning of trace elements in co-crystallized sphalerite–galena–chalcopyrite hydrothermal ores. *Ore Geol. Rev.* 77, 97–116. doi:10.1016/j.oregeorev.2016.02.009

Grammatikopoulos, T. A., Valeyev, O., and Roth, T. (2006). "Compositional variation in Hg-bearing sphalerite from the polymetallic Eskay Creek deposit, British Columbia, Canada,", 66. British Columbia, Canada, 307–314. doi:10.1016/j.chemer.2005.11.003*Geochemistry*

Hu, R. Z., Wei, W. F., Bi, X. W., Peng, J. T., Qi, Y. L., Wu, L. Y., et al. (2012). Molybdenite Re–Os and muscovite $^{40}Ar/^{39}Ar$ dating of the Xihuashan tungsten deposit, central Nanling district, South China. *Lithos* 150, 111–118. doi:10.1016/j.lithos.2012.05.015

Hu, X. L., Gong, Y. J., Pi, D. H., Zhang, Z. J., Zeng, G. P., Xiong, S. F., et al. (2017). Jurassic magmatism related Pb–Zn–W–Mo polymetallic mineralization in the central Nanling Range, South China: Geochronologic, geochemical, and isotopic evidence from the Huangshaping deposit. *Ore Geol. Rev.* 91, 877–895. doi:10.1016/j.oregeorev.2017.08.016

Huston, D. L., Sie, S. H., Suter, G. F., Cooke, D. R., and Both, R. A. (1995). Trace elements in sulfide minerals from eastern Australian volcanic-hosted massive sulfide deposits; Part I, Proton microprobe analyses of pyrite, chalcopyrite, and sphalerite, and Part II, Selenium levels in pyrite; comparison with delta 34 S values and implications for the source of sulfur in volcanogenic hydrothermal systems. *Econ. Geol.* 90, 1167–1196. doi:10.2113/gsecongeo.90.5.1167

Hutchison, M. N., and Scott, S. D. (1981). Sphalerite geobarometry in the Cu-Fe-Zn-S system. *Econ. Geol.* 76 (1), 143–153. doi:10.2113/gsecongeo.76.1.143

Jiang, H., Kong, H., Liu, B., Tan, F. C., Qin, Y. X., Huang, J. G., et al. (2024). Garnet and zircon U-Pb geochronology and geochemistry reveal genesis of the Dafang Au-Pb-Zn-Ag deposit, southern Hunan. *Acta Geol. Sin. Engl. Ed.* 98 (3), 717–735. doi:10.1111/1755-6724.15177

Johan, Z., Oudin, E., and Picot, P. (1983). Analogues germanifères et gallifères des silicates et oxydes dans les gisements de zinc des Pyrénées centrales, France: argutite et carboirite, deux nouvelles espèces minerales. *Tschermaks Petrogr. Mittl.* 31, 97–119. doi:10.1007/bf01084764

Keith, M., Haase, K. M., Schwarz-Schampera, U., Klemd, R., Petersen, S., and Bach, W. (2014). Effects of temperature, sulfur, and oxygen fugacity on the composition of sphalerite from submarine hydrothermal vents. *Geology* 42, 699–702. doi:10.1130/g35655.1

Keith, M., Haase, K. M., Chivas, A. R., and Klemd, R. (2022). Phase separation and fluid mixing revealed by trace element signatures in pyrite from porphyry systems. *Geochimica Cosmochimica Acta* 329, 185–205. doi:10.1016/j.gca.2022.05.015

Kelley, K. D., Leach, D. L., Johnson, C. A., Clark, J. L., Fayek, M., Slack, J. F., et al. (2004). Textural, compositional, and sulfur isotope variations of sulfide minerals in the Red Dog Zn–Pb–Ag deposits, Brooks Range, Alaska: implications for ore formation. *Econ. Geol.* 99 (7), 1509–1532. doi:10.2113/gsecongeo.99.7.1509

Li, X. M., and Li, G. S. (1983). Geological characteristics and ore controlling factors of Dafang lead-zinc polymetallic deposit in Guiyang County. *Hunan Geol.* 2 (1), 37–40.

Li, H., Yonezu, K., Watanabe, K., and Tindell, T. (2017). Fluid origin and migration of the Huangshaping W-Mo polymetallic deposit, South China: geochemistry and $^{40}Ar/^{39}Ar$ geochronology of hydrothermal K-feldspars. *Ore Geol. Rev.* 86, 117–129. doi:10.1016/j.oregeorev.2017.02.005

Li, R. C., Chen, H. Y., Xia, X. P., Yang, Q., Danyushevsky, L. V., and Lai, C. (2018). Using integrated *in-situ* sulfide trace element geochemistry and sulfur isotopes to trace ore-forming fluids: example from the Mina Justa IOCG deposit (southern Peru). *Ore Geol. Rev.* 101, 165–179. doi:10.1016/j.oregeorev.2018.06.010

Li, D. F., Tan, C. Y., Miao, F. Y., Liu, Q. F., Zhang, Y., and Sun, X. M. (2019). Initiation of Zn–Pb mineralization in the Pingbao Pb–Zn skarn district, South China: constraints from U–Pb dating of grossular-rich garnet. *Ore Geol. Rev.* 107, 587–599. doi:10.1016/j.oregeorev.2019.03.011

Li, B., Li, N. X., Yang, J. N., Zhang, W. D., and Liu, J. P. (2023). Genesis of the Xianghualing tin-polymetallic deposit in southern Hunan, South China: constraints from chemical and boron isotopic compositions of tourmaline. *Ore Geol. Rev.* 154, 105303. doi:10.1016/j.oregeorev.2023.105303

Liu, Y. J., Cao, M. L., Li, Z. L., Wang, H. N., and Chu, T. Q. (1984). *Geochemistry of element*. Beijing: Science Press, 1–548.

Liu, X., Wang, Q., Ma, L., Wyman, D. A., Zhao, Z. H., Yang, J. H., et al. (2020). Petrogenesis of late Jurassic Pb–Zn mineralized high $\delta^{18}O$ granodiorites in the western Nanling range, South China. *J. Asian Earth Sci.* 192, 104236. doi:10.1016/j.jseaes.2020.104236

Liu, S., Zhang, Y., Ai, G. L., Xue, X. L., Li, H. B., Sajjad, A. S., et al. (2022). LA-ICP-MS trace element geochemistry of sphalerite: metallogenic constraints on the Qingshuitang Pb–Zn deposit in the Qinhang Ore Belt, South China. *Ore Geol. Rev.* 141, 104659. doi:10.1016/j.oregeorev.2021.104659

Loftus-Hills, G., and Solomon, M. (1967). Cobalt, nickel and selenium in sulphides as indicators of ore genesis. *Miner. Deposita* 2, 228–242. doi:10.1007/bf00201918

Lu, Y. Y., Fu, J. M., Tan, S. M., Cheng, S. B., Guo, Z. Y., Qin, Z. W., et al. (2017). Geology and mineral Resources of South China, 133(3): 262–274.

Ma, Y., Jiang, S. Y., Frimmel, H. E., and Zhu, L. Y. (2022). *In situ* chemical and isotopic analyses and element mapping of multiple-generation pyrite: evidence of episodic gold mobilization and deposition for the Qiucun epithermal gold deposit in Southeast China. *Am. Mineralogist* 107, 1133–1148. doi:10.2138/am-2022-8030

Mao, J. W., Xie, G. Q., Guo, C. L., and Chen, Y. C. (2007). Large-scale tungsten-tin mineralization in the Nanling region, South China: metallogenic ages and corresponding geodynamic processes. *Acta Petrol. Sin.* 23, 2329–2338.

Mao, J. W., Xie, G. Q., Guo, C. L., Yuan, S. D., Cheng, Y. B., and Chen, Y. C. (2008). Spatial-temporal distribution of Mesozoic ore deposits in South China and their metallogenic settings. *J. China Univ. Geosciences* 14 (4), 510–526.

Mao, J. W., Chen, M. H., Yuan, S. D., and Guo, C. L. (2011). Geological characteristics of the Qinhang (or Shihang) metallogenic belt in South China and spatial-temporal distribution Regularity of mineral deposits. *Acta Geol. Sin.* 85, 636–658.

Mao, J. W., Cheng, Y. B., Chen, M. H., and Pirajno, F. (2013). Major types and time-space distribution of Mesozoic ore deposits in South China and their geodynamic settings. *Miner. Deposita* 48, 267–294. doi:10.1007/s00126-012-0446-z

Meinert, L. D. (1992). Skarns and skarn deposits. *Geosci. Can.* 19, 145–162. doi:10.12789/gs.v19i4.3773

Meinert, L. D., Dipple, G. M., and Nicolescu, S. (2005). World skarn deposits. Economic Geology. *100th Anniv.*, 299–336.

Paton, C., Hellstrom, J., Paul, B., Woodhead, J., and Hergt, J. (2011). Iolite: Freeware for the visualisation and processing of mass spectrometric data. *J. Anal. Atomic Spectrom.* 26, 2508–2518. doi:10.1039/c1ja10172b

Pattrick, R. A. D., Mosselmans, J. F. W., and Charnock, J. M. (1998). An X-ray absorption study of doped sphalerites. *Eur. J. Mineralogy* 10, 239–250. doi:10.1127/ejm/10/2/0239

Reich, M., Kesler, S. E., Utsunomiya, S., Palenik, C. S., Chryssoulis, S. L., and Ewing, R. C. (2005). Solubility of gold in arsenian pyrite. *Geochimica Cosmochimica Acta* 69 (11), 2781–2796. doi:10.1016/j.gca.2005.01.011

Rowins, S. M., Groves, D. l., McNaughton, N. J., Palmer, M. R., and Eldridge, C. S. (1997). A reinterpretation of the role of granitoids in the genesis of Neoproterozoic gold mineralization in the Telfer dome, Western Australia. *Econ. Geol.* 92, 133–160. doi:10.2113/gsecongeo.92.2.133

Schaarschmidt, A., Haase, K. M., Klemd, R., Keith, M., Voudouris, P. C., Alfieris, D., et al. (2021). Boiling effects on trace element and sulfur isotope compositions of sulfides in shallow-marine hydrothermal systems: evidence from Milos Island. Greece. *Chem. Geol.* 583, 120457. doi:10.1016/j.chemgeo.2021.120457

Scott, S. D., and Barnes, H. L. (1971). Sphalerite geothermometry and geobarometry. *Econ. Geol.* 66, 653–669. doi:10.2113/gsecongeo.66.4.653

Shen, H. J., Zhang, Y., Zuo, C. H., Shao, Y. J., Zhao, L. J., Lei, J. Z., et al. (2022). Ore-forming process revealed by sphalerite texture and geochemistry: a case study at the Kangjiawan Pb–Zn deposit in Qin-Hang Metallogenic Belt, South China. *Ore Geol. Rev.* 150, 105153. doi:10.1016/j.oregeorev.2022.105153

Shen, H. J., Zhang, Y., Pan, Z., Shao, Y. J., Brzozowski, M. J., Zhao, L. J., et al. (2025). Newly discovered early cretaceous Au mineralization overprinting late jurassic Pb-Zn-Ag mineralization in the Qin-Hang metallogenic belt (South China). *Geol. Soc. Am. Bull.* 137 (3-4), 1021–1036. doi:10.1130/b37691.1

Shu, L. S., Zhou, X. M., and Deng, P. (2004). Geological features and tectonic evolution of Meso-Cenozoic basins in Southeastern China. *Geol. Bull. China* 23, 876–884.

Shu, X. J., Wang, X. L., Sun, T., Xu, X., and Dai, M. N. (2011). Trace elements, U–Pb ages and Hf isotopes of zircons from Mesozoic granites in the western Nanling Range, South China: implications for petrogenesis and W-Sn mineralization. *Lithos* 127, 468–482. doi:10.1016/j.lithos.2011.09.019

Tan, F. C., Kong, H., Liu, B., Wu, Q. H., and Chen, S. F. (2023). *In situ* U-Pb dating and trace element analysis of garnet in the Tongshanling Cu polymetallic deposit, South China. *Minerals* 13, 187. doi:10.3390/min13020187

Tan, F. C., Kong, H., Liu, B., Wu, Q. H., and Yang, Q. Z. (2024). Timing and genesis of the Tongshanling stratiform W-Mo skarn deposit in Hunan Province: implications for exploration. *Bull. Geol. Sci. Technol.* 43 (2), 123–142.

Torró, L., Millán-Nuñez, A. J., Benites, D., González-Jiménez, J. M., Laurent, O., Tavazzani, L., et al. (2023). Germanium- and gallium-rich sphalerite in Mississippi Valley–type deposits: the San Vicente district and the Shalipayco deposit, Peru. *Miner. Deposita* 58, 853–880. doi:10.1007/s00126-023-01160-4

Voute, F., Hagemann, S. G., Evans, N. J., and Villanes, C. (2019). Sulfur isotopes, trace element, and textural analyses of pyrite, arsenopyrite and base metal sulfides associated with gold mineralization in the Pataz-Parcoy district, Peru: implication for paragenesis, fluid source, and gold deposition mechanisms. *Miner. Deposita* 54, 1077–1100. doi:10.1007/s00126-018-0857-6

Wang, K. X., Zhai, D. G., Liu, J. J., and Wu, H. (2021). LA-ICP-MS trace element analysis of pyrite from the Dafang gold deposit, South China: implications for ore genesis. *Ore Geol. Rev.* 139, 104507. doi:10.1016/j.oregeorev.2021.104507

Wang, K. X., Zhai, D. G., Zhang, L. L., Li, C., Liu, J. J., and Wu, H. (2022). Calcite U-Pb, pyrite Re-Os geochronological and fluid inclusion and H-O isotope studies of the Dafang gold deposit, South China. *Ore Geol. Rev.* 150, 105183. doi:10.1016/j.oregeorev.2022.105183

Wang, K. X., Zhai, D. G., William-Jones, A. E., Li, D. F., and Liu, J. J. (2023). Discrete late Jurassic Sn mineralizing events in the Xianghualing ore district, South China: constraints from cassiterite and garnet U-Pb geochronology. *Am. Mineralogist* 108, 1384–1398. doi:10.2138/am-2022-8412

Wei, C., Ye, L., Huang, Z. L., Gao, W., Hu, Y. S., Li, Z. L., et al. (2018). Ore genesis and geodynamic setting of Laochang Ag–Pb–Zn–Cu deposit, Southern Sanjiang Tethys Metallogenic Belt, China: constraints from whole rock geochemistry, trace elements in sphalerite, zircon U–Pb dating and Pb isotopes. *Minerals* 8, 516–529. doi:10.3390/min8110516

Wei, C., Ye, L., Hu, Y., Danyushevskiy, L., Li, Z., and Huang, Z. (2019). Distribution and occurrence of Ge and related trace elements in sphalerite from the Lehong carbonate-hosted Zn–Pb deposit, northeastern Yunnan, China: insights from SEM and LA-ICP-MS studies. *Ore Geol. Rev.* 115, 103175. doi:10.1016/j.oregeorev.2019.103175

Wen, H., Zhu, C., Zhang, Y., Cloquet, C., Fan, H., and Fu, S. (2016). Zn/Cd ratios and cadmium isotope evidence for the classification of lead-zinc deposits. *Sci. Rep.* 6, 25273. doi:10.1038/srep25273

Wu, J. H., Kong, H., Li, H., Thomas, J., Algeo, C. D. E., Kotaro, Y., et al. (2021). Multiple metal sources of coupled Cu-Sn deposits: insights from the Tongshanling polymetallic deposit in the Nanling Range, South China. *Ore Geol. Rev.* 139, 104521. doi:10.1016/j.oregeorev.2021.104521

Xia, J., Zhang, Z. Z., Lu, Y. Y., Li, J. F., Fu, J. M., Chen, X. Q., et al. (2024). Magma evolution sequence and genesis of the Qitianling pluton in Nanling Range. *Acta Geol. Sin.* 99 (5), 1606–1631.

Xiong, Y. Q., Shao, Y. J., Cheng, Y. B., and Jiang, S. Y. (2020). Discrete Jurassic and Cretaceous mineralization events at the Xiangdong W(–Sn) deposit, Nanling range, South China. *Econ. Geol.* 115, 385–413. doi:10.5382/econgeo.4704

Yao, Y., Chen, J., Lu, J. J., Wang, R. C., and Zhang, R. Q. (2014). Geology and genesis of the Hehuaping magnesian skarn-type cassiterite-sulfide deposit, Hunan Province, Southern China. *Ore Geol. Rev.* 58, 163–184. doi:10.1016/j.oregeorev.2013.10.012

Ye, L., Cook, N. J., Ciobanu, C. L., Yuping, L., Zhang, Q., Tiegeng, L., et al. (2011). Trace and minor elements in sphalerite from base metal deposits in South China: a LA-ICPMS study. *Ore Geol. Rev.* 39, 188–217. doi:10.1016/j.oregeorev.2011.03.001

Yuan, S. D., Peng, J. T., Shen, N. P., Hu, R. Z., and Dai, T. M. (2007). ^{40}Ar–^{39}Ar isotopic dating of the Xianghualing Sn-polymetallic orefield in Southern Hunan, China and its geological implications. *Acta Geol. Sin.* 81 (2), 278–286. doi:10.1111/j.1755-6724.2007.tb00951.x

Yuan, S. D., Williams-Jones, A. E., Mao, J. W., Zhao, P. L., Yan, C., and Zhang, D. L. (2018a). The origin of the Zhangjialong tungsten deposit, South China: implications for W–Sn mineralization in large granite batholiths. *Econ. Geol.* 113 (5), 1193–1208. doi:10.5382/econgeo.2018.4587

Zhang, J. K. (2023). *Petrogenesis and mineralization of the Baoshan Cu-Pb-Zn polymetallic deposit in Hunan province, South China. PhD thesis*. Central South University.

Zhang, P. F., and Wang, F. (2023). Characterization and genesis analysis of Dafang gold–silver polymetallic deposit in Guiyang County. *Nonferrous Met. Des.* 50 (4), 24–27.

Zhang, J. R., Yuan, S. D., Xuan, Y. S., and Zhang, D. L. (2018). Zircon U-Pb ages, Hf isotope and trace element characteristics of the granodiorite porphyry from the Baoshan-Dafang ore district, Hunan: implications for regional metallogeny. *Acta Petrol. Sin.* 34 (9), 2548–2564.

Zhang, Y., Chen, H. Y., Chen, J. M., Tian, J., Zhang, L. J., and Olin, P. (2022). Pyrite geochemistry and its implications on Au-Cu skarn metallogeny: an example from the Jiguanzui deposit, Eastern China. *Am. Mineralogist* 107, 1910–1925. doi:10.2138/am-2022-8118

Zhao, G. C., and Cawood, P. A. (2012). Precambrian geology of China. *Precambrian Res.* 222, 13–54. doi:10.1016/j.precamres.2012.09.017

Zhao, L. J., Zhang, Y., Shao, Y. J., Li, H. B., Shah, S. A., and Zhou, W. J. (2021). Using garnet geochemistry discriminating different skarn mineralization systems: perspective from Huangshaping W–Mo–Sn–Cu polymetallic deposit, South China. *Ore Geol. Rev.* 138, 104412. doi:10.1016/j.oregeorev.2021.104412

Zhao, L. J., Shao, Y. J., Zhang, Y., Li, H. B., and Shah, S. A. (2022). Differentiated enrichment of magnetite in the Jurassic W–Sn and Cu skarn deposits in the Nanling Range (South China) and their ore-forming processes: an example from the Huangshaping deposit. *Ore Geol. Rev.* 148, 105046. doi:10.1016/j.oregeorev.2022.105046

Zhao, H. T., Zhang, Y., Shao, Y. J., Liao, J., Song, S. L., Cao, G. S., et al. (2024). A New sphalerite thermometer based on Machine Learning with trace element geochemistry. *Nat. Resour. Res.* 33, 2609–2626. doi:10.1007/s11053-024-10408-3

Zhao, L. J., Shao, Y. J., Zhang, Y., Liu, L. Y., Zhang, S. T., Zhao, H. T., et al. (2024). Pyrite geochemical fingerprinting on skarn ore-forming processes: a case study from

the Huangshaping W–Sn–Cu–Pb–Zn deposit in the Nanling Range, South China. *J. Geochem. Explor.* 262, 107474. doi:10.1016/j.gexplo.2024.107474

Zhou, M. F., Yan, D. P., Kennedy, A. K., Li, Y. Q., and Ding, J. (2002). SHRIMP U-Pb zircon geochronological and geochemical evidence for Neoproterozoic arc-magmatism along the western margin of the Yangtze Block, South China. *Earth Planet. Sci. Lett.* 196, 51–67. doi:10.1016/s0012-821x(01)00595-7

Zhou, X. M., Sun, T., Shen, W. Z., Shu, L. S., and Niu, Y. L. (2006). Petrogenesis of Mesozoic granitoids and volcanic rocks in South China: a Response to tectonic evolution. *Episodes* 29, 26–33. doi:10.18814/epiiugs/2006/v29i1/004

Zhu, D. P., Li, H., Tamehe, L. S., Jiang, W. C., Wang, C., and Wu, K. Y. (2022). Two-stage Cu–Pb–Zn mineralization of the Baoshan deposit in southern Hunan, South China: constraints from zircon and pyrite geochronology and geochemistry. *J. Geochem. Explor.* 241, 107070. doi:10.1016/j.gexplo.2022.107070